University of Cape Town

Masters Thesis

Dispersion measure variations in pulsar observations with LOFAR

Author:
Abubakr Ibrahim

Supervisors:
Dr Maciej Serylak
Dr Shazrene Mohamed

A thesis submitted in fulfilment of the requirements for the degree of MSc (Astrophysics)

in the

Faculty of Science
Department of Astronomy

April 2019

Declaration of Authorship

I, Abubakr Ibrahim, declare that this thesis titled, 'Dispersion measure variations in pulsar observations with LOFAR' and the work presented in it is my own. "I confirm that this work submitted for assessment is my own and is expressed in my own words. Any uses made within it of the works of other authors in any form (e.g., ideas, equations, figures, text, tables, programs) are properly acknowledged at any point of their use. A list of the references employed is included".

Signed: Signed by candidate

Date:

"Not only are we in the universe, the universe is in us. I don't know of any deeper spiritual feeling than what that brings upon me."

Neil deGrasse Tyson, Astrophysicist

UNIVERSITY OF CAPE TOWN

Abstract

Faculty of Science
Department of Astronomy

MSc (Astrophysics)

Dispersion measure variations in pulsar observations with LOFAR

by Abubakr Ibrahim

I present an analysis of the dispersion measure (DM) variations for 68 pulsars. The observations were taken using six International LOFAR Stations in Europe over the period of 3.5 years (between June 2014 and November 2017) at the centre frequency of 150 MHz with 80 MHz of bandwidth. During this time each pulsar was observed on weekly basis resulting in an average of 160 observations per source. I show that, the variations of the DM measurements show various trends along the span of the observation: increasing or decreasing, and in some cases more changes from one trend to another. I perform the structure function analysis for each of observed pulsar included in the study, in order to check if the DM variations follow the Kolmogorov power spectrum which describes the turbulence structure of the interstellar medium (ISM). I find that for a number of pulsars results show consistency with the Kolmogorov distribution (e.g. PSRs J1913−0440 and J2157+4017) while other sources show significant difference (e.g. PSRs J0108+6608 and J0614+2229). I also obtain the DM derivatives (i.e. dDM/dt) for each pulsar, in order to examine the correlation between the DM and its derivative. The result of this correlation shows a best-fit with a square-root dependence of 0.6±0.2, which is comparable with the result that was previously obtained by Hobbs et al. (2004), who shows a dependence of square-root between the DM and its derivative; with a gradient of 0.57±0.09. Also, one of the major results of this study that, thanks to the timing analysis, allowed me to produce a new timing solution for three pulsars: PSRs J0613+3731, J0815+4611 and J1740+27. This study concludes in that: i) the DM variations can be used to understand the general properties of the ISM ii) the low-frequency observations can enable us to study the dispersion effect on pulsar signals, which can be very useful for the effort of the pulsar timing array (PTA) project iii) IISM studies using pulsar timing is a powerful technique requiring careful approach to data reduction and analysis due to characteristic of the pulsars.

Acknowledgements

First of all, I would like to express my deepest appreciation to my supervisor Dr Maciej Serylak, for giving me an opportunity of working in this wonderful project, and for his patient, guidance and generosity for being always available for me during the entire period of the project. I would also like to extend my deepest appreciation to my co-supervisor Dr Shazrene Mohamed, for her numerous efforts on taking care of all the official and scientific inputs, and making sure the project is flowing smoothly even during the leave. I'm also grateful to all the members of EPTA IISM group for their useful inputs, comments, and help throughout the project. Especially, I'm extremely grateful to Dr Caterina Tiburzi for her incredible willingness in helping me every time I need it. Special thanks to Dr Marisa Geyer for being a very kind and generous person in helping me in all the aspects during the period of my project. I also want to thanks Dr Lucas Guillemot, Prof. Joris Verbiest, Dr James McKee, Dr Jean-Mathias Griessmeier, Sarah Buchner and Prof. Aris Karastergiou, for their help and valuable comments. I want to thanks my colleague Isabella Rammala for the fabulous environment and for being so helpful when we chat about pulsars. Thanks, Issac for the accompany and all my NASSPies colleagues. I gratefully acknowledge: the National Astrophysics and Space Science Program (NASSP) for the generous funding of my project, and the International LOFAR Stations: FR606, SE607, DE601, DE602, DE603, and DE605, for providing me with the data. I'd like to recognize the supports of the Square Kilometer Array South Africa (SKA SA) office and the South African Astronomical Observatory (SAAO) for hosting my project and providing me with the necessary equipment to complete my research study. Finally, grateful thanks to my lovely family and friends for always being supportive all the time.

Contents

List of Figures

List of Tables

This thesis is dedicated to ...

The sake of Allah, my Creator and my Master;

My Parents: Yagob & Shama;
My lovely Sisters, Brothers and my Friends.

Chapter 1

Introduction

The interstellar medium (ISM) is the matter, radiation and magnetic fields that occupy the space between the stellar systemss in a galaxy. When the radio emission from a pulsar reaches an observer on Earth, it has propagated through different components of the ISM. Throughout this propagation, the emission from pulsar interacts with the free electrons in the ionized gas of the ISM. As a result, three main effects of the ISM on the emission from pulsars can be observed. These effects are scattering, scintillation and dispersion (e.g. Lorimer and Kramer 2005).

The last mentioned case i.e. dispersion, can be seen clearly in the frequency-resolved pulse profile from radio pulsars. This effect is best noticeable in delay between emitted pulses at lower frequencies, which arrive later, and the pulses emitted at the higher frequencies (e.g. Figure 1.1). The so-called *dispersion measure* (DM) denotes the amount of ionised ISM between a pulsar and an observer. It also determines the delay time between pulse received at higher frequency compared with its lower frequency counterpart.

The main purpose of this thesis is to obtain DM variations for a large sample of pulsars observed with six International LOFAR Stations located in Europe with aim to understand the general properties of the ISM. These observations were made for 68 pulsars over the period between June 2014 and November 2017 ($\sim$ 3.5 years).

By obtaining DM measurements from low-frequency observations, where the dispersive effect of the ISM is very pronounced, this project provides an important opportunity to study the time-dependent DM changes of the ISM structure with high precision due to their high cadence. This is essential for many aspects of pulsars science e.g. studying the general properties of the interstellar medium and its effect on the radio emission from pulsars. With the ultimate goal of the Pulsar Timing Arrays (PTAs)

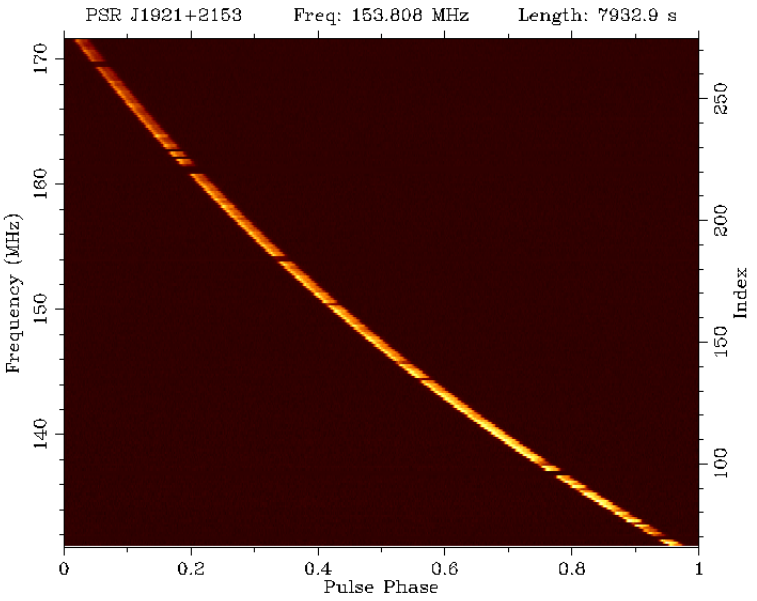

FIGURE 1.1: The effect of the ISM dispersion on the received signal from PSR J1921+2153. The plot shows the dispersion in the frequency profile, where the received pulse at lower frequencies arrive later than the emitted pulses at the higher frequencies. The gaps along the pulses of this plot are removed frequency channels due to RFI. This pulsar is included in this study.

projects aiming to detect the stochastic gravitational waves (GWs) background using so-called high-precision pulsar timing, precisely characterizing DM using low-frequency observations, similar to those used in this study, can greatly improve pulsar timing at higher frequencies. Such study was shown in Cordes et al. (2016), where the analysis of the frequency dependence of the DM showed rms DM difference of $\sim 4 \times 10^{-5}$ pc cm^{-3} across number of frequency bands near 1.5 GHz for pulsars at $\sim$ 1 kpc distance. The obtained arrival-time variations were ranged as: i) from few to hundreds of nanosecond for DM $\leq$ 30 pc cm^{-3} (with rapidly increasing to microseconds) ii) more than hundreds nanosecond for larger DM as well as wider frequency bands.

This thesis is divided into five chapters as follows:
Chapter 2 contains five sections, wherein the first section I present an overview about pulsars and their first discovery and their distribution. In the second and third sections, I show the basic properties of pulsars and their main categories, respectively. In the fourth section, I introduce the interstellar medium and its effects on the pulsar observations. While in section five I present the concept of pulsar timing.
Chapter 3 is split into three sections. The first section introduces the Low-Frequency Array (LOFAR) telescope with a brief description of its components and its functionality. A full description of the data used in this thesis and their reduction is introduced in the

second and third section respectively.

Chapter 4 contains two sections. In the first section, I give a detailed description of the data analysis. The results and the outcomes of this study are presented in the second section.

Chapter 5 contains of the conclusion and the discussion of the study.

Chapter 2

Pulsars and Neutron Stars

Pulsars are highly magnetized and rapidly rotating neutron stars which emit across a wide range of wavelengths. Most pulsars are observed in the radio part of the electromagnetic spectrum, but some also known to emit at optical wavelengths, X-rays and gamma-rays. Their radiation can be observed when a beam of emission crosses the path toward observer. In this Chapter, the discovery of pulsars is presented in § 2.1. The basic properties of pulsars are given in § 2.2, and their population in § 2.3. The interstellar medium and their effects on pulse propagation are presented in § 2.4, and a brief overview of pulsar timing is also given in § 2.5.

2.1 Discovery

The discovery of the pulsars was made by Jocelyn Bell in July 1967 (Hewish et al., 1968), while she was investigating the scintillation of radio signals from quasars caused by the irregular structure of the interplanetary medium (e.g. Figure 2.1). This investigation was carried out with the Mullard Radio Astronomy Observatory which operated at a frequency of 81 MHz. Four months later in November, after systematic investigation and analysis a very stable pulse signal with a period of 1.337 seconds was revealed. The nature of this signal was first considered to be an extra-terrestrial intelligence signal or terrestrial signal reflected off the Moon, but none of these theories was accepted. Instead, the authors stated that:"*A tentative explanation of these unusual sources in terms of the stable oscillations of white dwarf or neutron stars is proposed*".
In 1934, two astronomers, Walter Baade and Fritz Zwicky, suggested a new type of star as a result of the supernova explosion of a massive star (Baade and Zwicky, 1934). Since then, many studies (e.g Oppenheimer and Volkoff, 1939) have supported this model. In their study, Oppenheimer and Volkoff used the equation of state (EoS) for a cold Fermi

gas, to show that a quasi-static solution is required to interpret the collapse of a large mass into a small and dense core. This ultimately enabled them to predict the density and the total mass of the resulting star. In 1967, Pacini (1967) also suggested that a high dense stellar core with a strong magnetic field could be the product of a supernova explosion and as the result, it could be the source of the energy in the Crab Nebula. These studies indicate that a spinning neutron star could be the origin of the discovered pulsar.

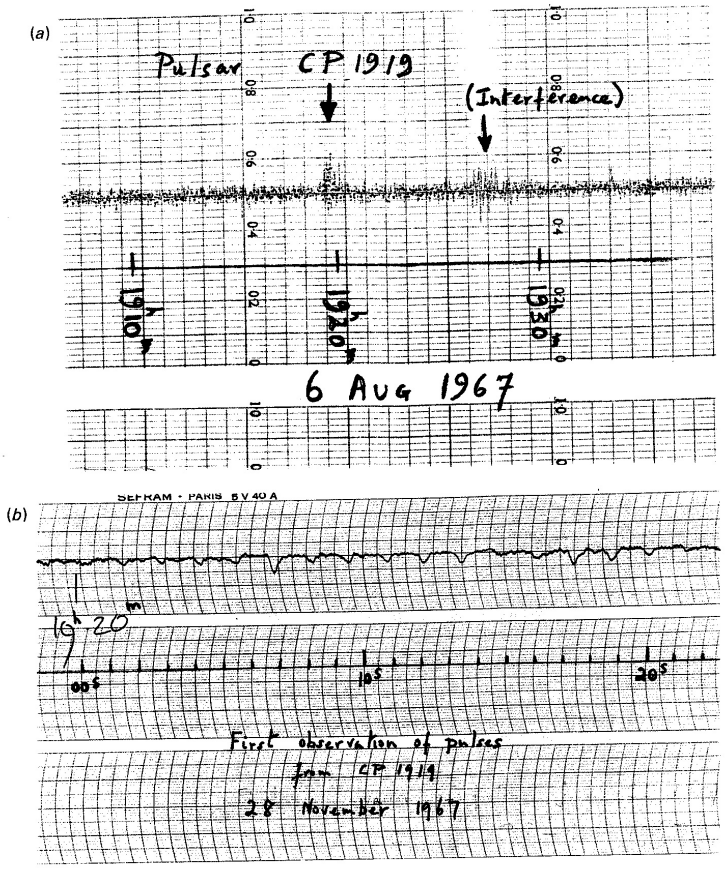

FIGURE 2.1: The observation of the first discovered pulsar. (a) The first recording of PSR 1919+21; initially the signal resembled the radio interference also seen on this chart. (b) Fast chart recording showing individual pulses as downward deflections of the trace (Hewish et al., 1968).

2.2 Pulsar and Neutron Star Properties

In this section, a general overview of pulsar properties will be introduced in § 2.2.1. Also, a brief description of the rotating dipole model, which attempts to explain the mechanism of pulsar emission, will be given in § 2.2.2, and pulsar distribution within the Galaxy will be presented in § 2.2.3.

2.2.1 Basic Properties

- **Mass**

  The properties of the neutron stars can be deduced by using the equation of state (EoS), given by Oppenheimer and Volkoff (1939). Based on EoS models, the maximum mass of the neutron star is predicted to be about 2 $M_\odot$ (Lattimer and Prakash, 2001; Lorimer and Kramer, 2005). The maximum values of the neutron star masses differ in the literature. For example, Lyne and Graham-Smith (2012) have shown, based on the current theory, the possible maximum value of 3 $M_\odot$ for the mass of neutron star.

- **Radius and density**

  As shown by Lyne and Graham-Smith (2012), the masses of neutron stars in binary systems can be measured with high accuracy (currently $\sim$ 280 binary system[1]). This leads to an average neutron star mass of 1.35 $M_\odot$ for most measurements of the mass. The range of masses between 0.5 and 2 $M_\odot$ in their study using the EoS models gives an equivalent radius range of between 10.5 and 11.2 km.

  Consequently, the upper limit on the radius of the neutron star can be deduced by taking into account the stability of the neutron star due to the centrifugal force. For neutron star with mass M, radius R, and rotating with angular velocity Ω, and considering the period, $P = 2\pi/\Omega$, the radius can be given in the form:

$$R = 1.5 \times 10^3 \left(\frac{M}{M_\odot}\right)^{1/3} P^{2/3}\text{km}. \tag{2.1}$$

  For the fastest known pulsar, PSR J1748−2446ad with a period of $P = 1.40$ ms ($\sim$ 716 Hz or rotations per second, Hessels et al., 2006), and by considering the mass $m = 1.35$ $M_\odot$, this gives an upper limit radius of $R = 21.5$ km.

  By assuming mass and radius for a neutron star to be $M = 1.4$ $M_\odot$ and $R = 10$ km respectively, its mean density is estimated to be $\rho = 6.7 \times 10^{14}$ cm^{-3} (Lyne and Graham-Smith, 2012).

- **Spin-down luminosity**

  The loss of rotational kinetic energy is considered to be the reason for the observed spin down of the neutron star. The reason for this energy lost is due to the emitted magnetic dipole radiation from radio pulsars. The effect of this appears as an increase of pulse period of the pulsar as,

$$\dot{P} = \frac{dP}{dt}. \tag{2.2}$$

[1] http://www.atnf.csiro.au/research/pulsar/psrcat/

Where $\dot{P}$ is known as the period derivative, which is dimensionless (seconds per second).

The loss of energy can be defined as,

$$\dot{E} \equiv -\frac{dE_{rot}}{dt} = -I\Omega\dot{\Omega}, \tag{2.3}$$

where $\Omega = 2\pi/P$ is the rotational angular frequency and I is the moment of inertia of the neutron star ($I = 10^{45}$ g cm^2). This equation defines the total emitted power from the neutron star.

- **Spin down and characteristic ages**

  The spin down model can be further expressed in terms of rotational frequency ($f = 1/P$) by

$$\dot{f} = -Kf^n. \tag{2.4}$$

  where K is constant and n is the so-called "breaking index" (denotes the spin-down behavior of the star, in the general case, $n \sim 3$).

  Equation (2.4) can be expressed in terms of the pulse period as,

$$\dot{P} = KP^{2-n}. \tag{2.5}$$

  This is a first-order differential equation and therefore, by integrating it and assuming K is a constant and $n \neq 1$ (from Equation (2.4)), the age of the pulsar can be approximated as,

$$T = \frac{P}{(n-1)\dot{P}}\left[1 - \left(\frac{P_0}{P}\right)^{n-1}\right], \tag{2.6}$$

  where P_0 represents the spin period at the birth of the star. We can simplify Equation (2.6) by assuming $P_0 << P$, and assuming that the spin-down is only caused by the magnetic dipole radiation, $n = 3$, as follows,

$$\tau = \frac{P}{2\dot{P}} \quad . \tag{2.7}$$

- **Magnetic field**

  The magnetic moment can be related to the magnetic field strength as $B \approx \frac{|m|}{r^3}$, where $|m|$ is the magnetic moment and r is the radius. Assuming the neutron star has radius $R = 10$ km and the moment of inertia $I = 19^{45}$ g cm^2; we can

determine the magnetic field of a pulsar in terms of its period and period derivatives as follows,

$$B = 3.2 \times 10^{19} G \sqrt{P\dot{P}}. \tag{2.8}$$

Where G is the Newton's gravitational constant, P is the pulse period and $\dot{P}$ is the period derivative.

2.2.2 Rotating Dipole Model

Although the emission mechanism of the pulsars is not yet fully understood, many models trying to explain it have been proposed. One of the first model was put forward by Goldreich and Julian (1969). In this model, the neutron star was assumed to have a dense magnetosphere where the particles will be electrostatically accelerated along the strong magnetic field lines. Then, due to the acceleration, these particles gain energy and escape through the open field lines (e.g. Figure 2.2).

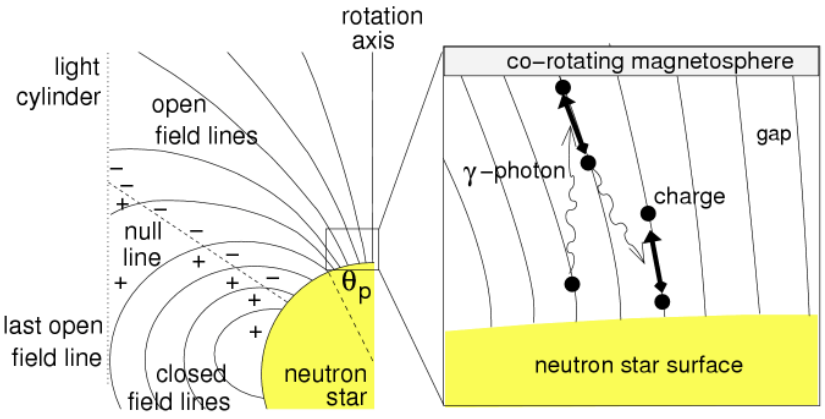

FIGURE 2.2: Diagram presenting the Goldreich-Julian model. Showing the pulsar magnetosphere that contains a polar gap with the electron-positron cascades. Figure taken from Handbook of Pulsar Astronomy by Lorimer and Kramer (2005).

Following the model of Goldreich and Julian (1969), another attempt was carried out by Sturrock (1971). He proposed a new model of "polar caps". The polar caps are the areas where the open field lines reach the light cylinder and connect with the surface of the star in Figure 2.2. The electrons are accelerated along the open magnetic field lines which leads to the production of a γ-ray emission due to the curvature radiation. If the pulsar has a short period ($P < 1$ second), electron-positron pairs will be generated and accelerated for the second time to produce more emission in the form of a pair cascade. Ruderman and Sutherland (1975) proposed an improved model, the so-called "polar

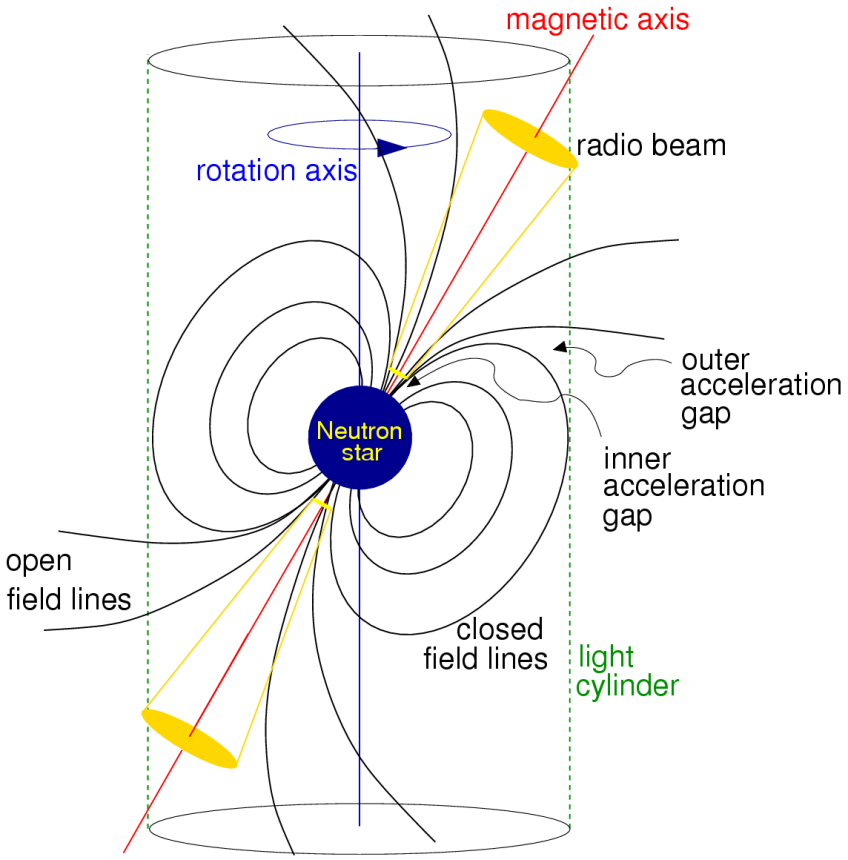

FIGURE 2.3: The rotating dipole of the pulsar emission of the polar gap model. The pairs of electrons-positrons are accelerated through the "gap" regions of the magnetosphere. The pairs then escape along the open magnetic fields lines to emit two beams of radiation. Figure taken from Handbook of Pulsar Astronomy by Lorimer and Kramer (2005).

gap" model, which expands on the previous model, by suggesting that the open field lines are extended to a high altitude from the stellar surface by the polar magnetosphere gap. This creates a potential difference of 10^{12} volts between the top and the base of the gap, as a result, the gap "spark" by generating electron-positron pairs which in turn are responsible for the emission (e.g. Figure 2.3).

2.2.3 The Galactic Distribution

The standard model of neutron star formation proposed that neutron stars are the result of supernova explosions of the massive stars (Lyne and Lorimer, 1994). When a main sequence star, with mass $m \geq 10\ M_{\odot}$, explodes, it leaves a stable core that is supported against the gravitational collapse by so-called neutron degeneracy pressure (i.e. Type II supernova) which gives birth to a *neutron star*. The newly created neutron star has

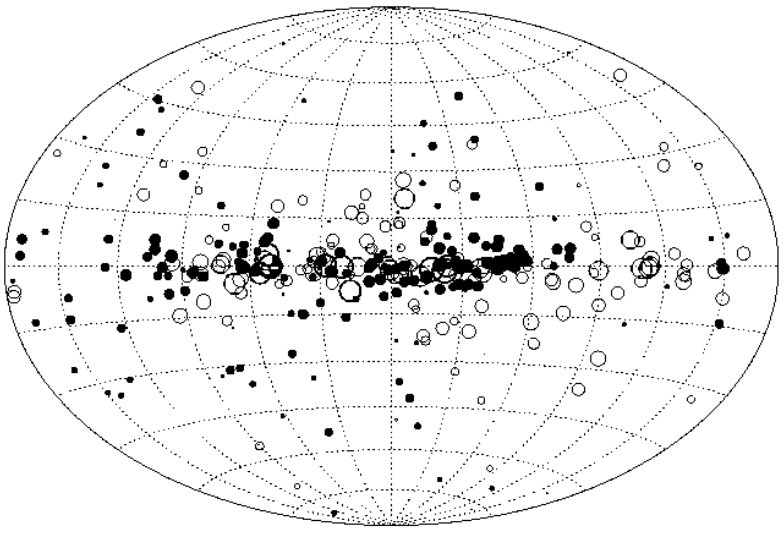

FIGURE 2.4: The distribution of pulsars across the galactic plane. The filled circles show the pulsars associated with the supernova while the open circles show the millisecond pulsars, plotted in the Hammer-Aitoff projection of the sky in Galactic coordinates. Figure taken from Handbook of Pulsar Astronomy (Lorimer and Kramer, 2005).

an extremely high spin rate and magnetic field strength resulting from the conservation of the angular momentum and the magnetic flux during the collapse (Harding, 2013). Figure 2.4 indicates that most pulsars are located near the galactic plane which supports the standard model of neutron stars formation. This is mainly because of the high density of gas and matter in the galactic plane, which makes it a suitable environment for the star formation. More than 2600 pulsars are now known, with the full list available via the Australia Telescope National Facility (ATNF) Pulsar Catalogue[2].

To study the properties of pulsars, Gunn and Ostriker (1970) conducted a statistical study of pulsar height above and below the Galactic plane (z). This study leads to the first suggestion of the high-velocity motion of pulsars. By analyzing the pulsar observations in line with the magnetic-dipole model, they found that pulsars are likely born with large velocities, which agreed with the previous dynamic hypothesis. This implies a "kick" with a velocity of a few hundred km s^{-1} during the birth. Similarly, it explains why the young pulsars are close to plane while the old luminous pulsars with very long periods appear far away from the Galactic plane with an isotropic distribution (see the open circles in Figure 2.4).

2.3 Pulsar Categories

Based on their observations and physical properties, pulsars have a very diverse population. In this section, a general overview of pulsars categories with their physical

[2] http://www.atnf.csiro.au/research/pulsar/psrcat/

properties and evolution paths is given.

2.3.1 P-$\dot{P}$ Diagram

The observed emission from pulsars, which is a result of the rotational kinetic energy loss of the neutron star, enables us to measure the pulsar spin period, P, and the corresponding spin-down rate, $\dot{P}$, to a very high precision. Using an idea similar to the Hertzsprung-Russell diagram which is used to classify different type of stars, the P-$\dot{P}$ diagram gives us an excellent overview of the spin evolution of the neutron stars. Figure 2.5 presents a P-$\dot{P}$ diagram[3] with various classes of neutron stars. It includes the ordinary pulsar population (see the black dots in Figure 2.5 magnetars; including soft gamma repeaters and anomalous X-ray pulsars (SGR/AXP), the binary systems which are the origin of the millisecond pulsars, pulsars associated with supernova remnants (SNR), rotating radio transients (RRATs), pulsars with radio-infrared emission and sources with pulsed thermal X-ray emission.

2.3.2 Normal Pulsars

From the diagram in Figure 2.5 it's clear that normal pulsars have surface magnetic field strengths of the order of 10^{11} – 10^{13} G, spin periods of 0.1 – 1.0 second and period derivatives of the order of 10^{-16} – 10^{-14} s s^{-1}. The normal pulsars have a short spin period when they form, followed by a spin down phase. As a result, they move toward the central so-called "pulsar island" with characteristic ages of 10^5 – 10^8 yr until finally, they become too faint to be detected after 10^8 yr. More information about the characteristics of normal pulsars can be found in Wielebinski (2002).

2.3.3 Millisecond Pulsars (MSPs)

The second class of the neutron star population are Millisecond Pulsars (MSPs). They are classified as rotation-powered pulsars with very short periods ($P = 1 - 30$ ms), low period derivatives ($\dot{P} \leq 10^{-19}$) and very stable spin-down rates. With these characteristics, millisecond pulsars are considered as valuable tools for pulsar timing measurements. As we look at Figure 2.5, we can clearly spot the millisecond pulsar population in the bottom left of the P-$\dot{P}$ diagram, with magnetic field of about 10^8 G and characteristic ages starting from 10^7 yr. One of the main properties of millisecond pulsars is that they

[3]The diagram is created by using **psrqpy package**, that queries the present known pulsars from ATNF catalogue. For more details about psrqpy see `https://psrqpy.readthedocs.io/en/latest/` and Pitkin (2018)

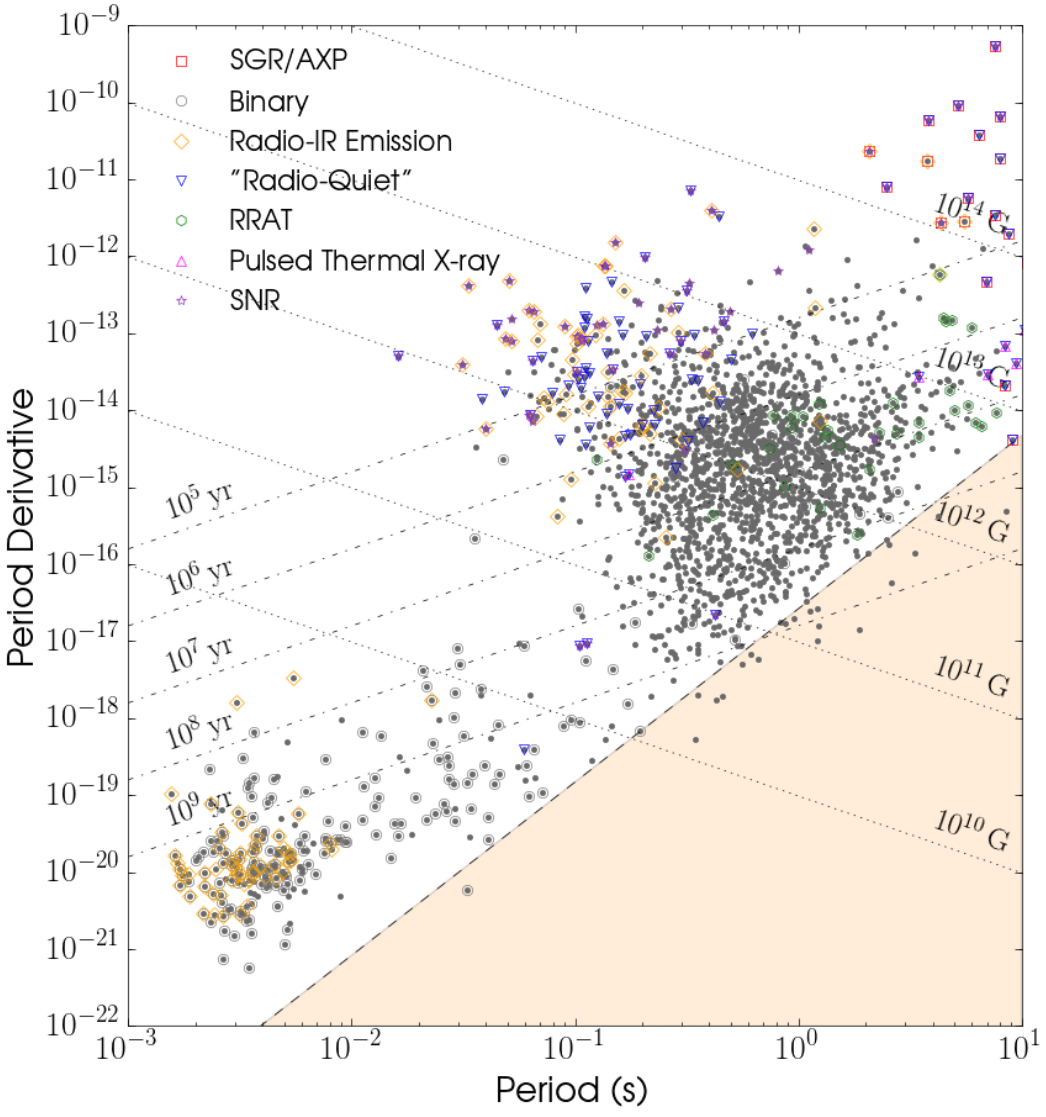

FIGURE 2.5: The P-$\dot{P}$ diagram for the currently known: Magneters (SGR/AXP); pulsars in binary system (Binary); pulsars with radio-infrared emission, radio-quiet neutron stars; Rotating Radio Transients (RRATs); Radio-Quiet; Pulsed Themal X-ray and pulsars associated with supernova remnants (SNR) (from http://www.atnf.csiro.au/people/pulsar/psrcat/). The diagram also include crossed lines which are used to determine the characteristic age (dot-dash lines) and the magnetic fields of the population (dotted lines).

have orbiting companions, observed in $\sim 80\%$ of the total number of millisecond pulsars (compared to $\sim 1\%$ for the normal pulsars). These orbiting companions could be either a main sequence star, a white dwarf or a neutron star.

The formation and evolutionary model for different binaries is shown in Figure 2.6. During the spin-down phase of pulsars in binary systems, they remain bound to the companion. Then the companion starts to expand and evolve to become a giant star. As a result, the distance between the pulsar and its companion will decrease which enables the companion to fill its Roche Lobe and subsequently, transfer the orbital momentum into the neutron star via an accretion disk. Next, the pulsar is spun up to a very short rotation period. This process creates a millisecond pulsar with a very low slow-down rate, so-called "recycled pulsar". At this stage, the X-ray emission will commence and the system is called an X-ray binary.

Depending on the mass of the companion, two classes can be identified: i) high-mass X-ray binaries (HMXBs) and ii) low-mass X-ray binaries (LMXBs). In the case of the HMXBs shown in Figure 2.6, if the binary is not disrupted in the process of the supernova explosion, it will become a double neutron star (DNS, see bottom right part of Figure 2.6). Example of such a system is PSR B1913+16, which was reported by Taylor and Weisberg (1982). The PSR J0737−3039 system (Burgay et al., 2003) is the first-known double pulsar system where the two pulsars were observed with a period of 22 ms for A and $\sim$ 2.8 s for B, and the orbital period between the two companions is equal to 2.4 hours. This makes it one of the best system to be used for testing the theory of general relativity. HMXBs can also form a neutron star-black hole binary or even a black hole binary, none of which has been discovered yet.
For the LMXBs case, the system evolves to be a millisecond pulsar-white dwarf binary system. For a full review see (Lorimer, 2001 and Backer et al., 1982).

2.3.4 Magnetars

Magnetars are a type of neutron star with an ultra-high magnetic field (i.e. $10^{14} - 10^{16}$ Gauss). As suggested in the magnetar model by Duncan and Thompson (1992), the decay of the magnetic field is the main source of the energy: "*The magnetic fields can deposit an enormous amount of energy outside a young neutron, and can catalyze the conversion of energy from neutrinos to electron pairs*".

Depending on their observed emissions, two classes of magnetars are recognized: i) Soft Gamma Repeaters (SGRs) which are identified as high-energy transient sources, and ii) rapidly spinning Anomalous X-ray Pulsars (AXPs) which show continuing pulsation in X-rays, with some of the sources exhibiting SGR-like bursts (denoted by red squares in

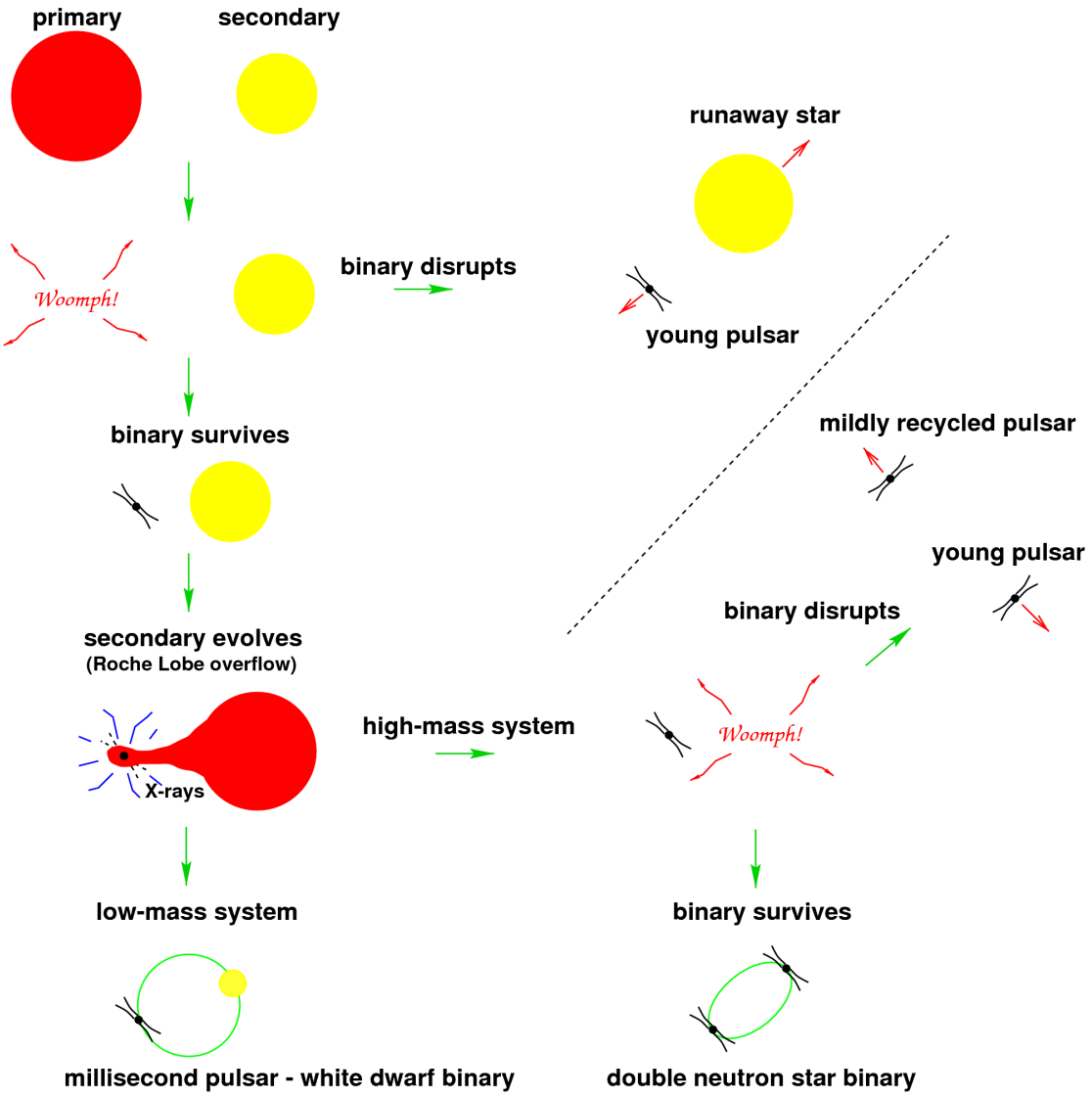

FIGURE 2.6: The formation and evolution of different types of binary systems. The image taken from (Lorimer, 2001).

top right of Figure 2.5).

These two classes have spin periods between 5 and 12 seconds and very young characteristic ages of the order $P/\dot{P} \sim 10^3 - 10^5$ yr. (for full review see: Lewin and Van der Klis, 2006). Magnetars have also been observed as a radio pulsar for the first time in the system XTE J1810−197 by Camilo et al. (2006). The system was found to emit bright and narrow radio pulses with a very high linear polarization fraction. Currently, a total of 29 magnetars are known (15 SGRs and 14 AXPs), whose details are listed in the McGill Online Magnetar Catalog[4] (see also Olausen and Kaspi, 2014).

[4] http://www.physics.mcgill.ca/~pulsar/magnetar/main.html

2.3.5 Rotating Radio Transients (RRATs)

Another class of neutron star was identified as the Rotating Radio Transients (RRATs). The discovery of RRATs was presented by McLaughlin et al. (2006). The authors described eleven sources identified through their single pulses of radio emission using data from the Parkes Multi-beam Pulsar Survey (PMPS) recorded between January 1998 and February 2002. The sources were characterized by short radio bursts of durations between 2 and 30 ms. The average time intervals between bursts range between 4 minutes and 3 hours. Later, each source was re-observed and showed a number of pulses (between 4 and 229 from each source with a period ranging from 0.4 to 7 second) and renamed as Rotating Radio Transients (RRATs).

As appears in Figure 2.5, RRATs have characteristic age $\tau \geq 10^7$ yr (the green hexagons shape at the top right of the figure). Currently, more than 100 sources are identified including the recent discovery of 25 RRATs (see Tyul'bashev et al., 2018). For further details see Keane (2010) and Harding (2013). The detailed properties of RRATs can be found in the RRATalog[5].

2.4 Interstellar Medium (ISM)

The interstellar medium (ISM) is the environment between the star systems in a galaxy that contains ordinary matter, relativistic charged particles (cosmic rays) and magnetic fields. The standard model consists of three components which are in pressure equilibrium. Two of these components were suggested by Field et al. (1969) based on the heating by low-energy cosmic rays. i) the cold dense phase, $T < 300K$, which consists of neutral and molecular hydrogen clouds and ii) the warm intercloud phase, $T = 10^4K$, consisting of ionized gas. The third phase is the hot ionized gas with a temperature of $T = 10^6K$ added by McKee and Ostriker (1977). Their study showed that the hot ionized gas is a result of the supernova explosions which create shock-waves that evaporate the cool clouds to a hot medium.

As the radio emission from pulsars propagates through the ionized interstellar medium (IISM), it interacts with the free electrons, leading to observable propagation effects. There are three main effects that can influence the pulsar signals while they travel through the IISM: scintillation, scattering, and dispersion. In order to be able to observe pulsars, one needs to correct for these effects (e.g. Armstrong et al., 1995).

[5] http://astro.phys.wvu.edu/rratalog/

2.4.1 Dispersion

As was mentioned earlier, the dispersion of a pulsar signal is one of the important characteristics of the ISM. The refractive index (n) of the ionized gas can be obtained from the plasma frequency f_p as follows,

$$n = \left(1 - \frac{f_p^2}{f^2}\right)^{1/2}. \tag{2.9}$$

Note that, the electron density, n_e, in ISM environment is given in cm^{-3}. As the approximate value of $n_e = 0.03$ cm^{-3} gives a plasma frequency, f_p, of 1.5 kHz, then we can approximate the refractivity $(n-1)$ to be -2.4×10^{-10} for a frequency, f, of 100 kHz. See Lyne and Graham-Smith (2012) for full explanation.

The plasma frequency in Equation (2.9) can be obtained as,

$$f_p = \sqrt{\frac{n_e e^2}{\pi m_e}} \simeq 8.5 kHz (\frac{n_e}{cm^{-3}})^{1/2}, \tag{2.10}$$

where n is the refractive index of the ionized gas and f is the frequency of the wave, e and m are the electronic charge and mass respectively. Since the group velocity of the traveling pulses is $\nu_g = cn$, where c is the speed of light in vacuum, thus for the given electron densities, the group velocity is

$$\nu_g^2 = c\left(1 - \frac{n_e e^2}{\pi m_e f^2}\right). \tag{2.11}$$

The travel time T through the distance L, therefore, will be in the form

$$T = \int_0^L \frac{dl}{v_g} = \frac{L}{c} + \frac{e^2 \int_0^L n_e dl}{2\pi mcv^2} = \frac{L}{c} + 1.345 \times 10^{-3} v^{-2} \int_0^L n_e dl \tag{2.12}$$

This equation shows the travel time in vacuum (the first term) with an additional term which represents the dispersive delay t. The extra term contains the dispersion measure (DM) given as follows,

$$DM = \int_0^L n_e dl. \tag{2.13}$$

The DM measures the electron density between the pulsar and the observer, with units cm^{-3}pc.

From Equation (2.12) and (2.13), the delay due to dispersion can be written in the form,

$$t = \mathcal{D} \times \frac{DM}{f^2}, \tag{2.14}$$

where $\mathcal{D}$ is the dispersion constant which can be given as,

$$\mathcal{D} = \frac{e^2}{4\pi mc} = 4.1488 \times 10^3 \mathrm{MHz}^2 \mathrm{pc}^{-1} \mathrm{cm}^3. \tag{2.15}$$

If we have two different frequencies (f_{low} and f_{high}), then Equation (2.14) can be written in another useful form as,

$$\Delta t = \mathcal{D} \times DM \times \left(\frac{1}{f_{low}^2} - \frac{1}{f_{high}^2} \right). \tag{2.16}$$

The effect of this delay can be seen in the observations when the pulses with higher frequencies arrive earlier than those in low frequencies (e.g. Figure 2.7). The time differences of the received signal with bandwidth B (in MHz) can be calculated (in seconds) as

$$\Delta t = 8.3 \times 10^3 DM f^2 B \tag{2.17}$$

2.4.2 Scattering

Another effect of the interstellar medium in pulsar signals is so-called scattering. The inhomogeneities in the electron density along the line of sight scatter the radio pulses. The combined effect of the inhomogeneities on the observed pulses is the broadening of pulses in time. To characterize this effect, a simple model of a thin screen was proposed by Williamson (1972), where the scattered radio waves along the line-of-sight from the pulsars to an observer lead to frequency-dependent effects such as the pulse broadening, (e.g. Figure 2.8).

As the wave propagates through an inhomogeneity (with scale a), its phases change due to the refractive index and thus, by considering a screen midway between the pulsar and the observer, we can identify this phase change $\Delta\phi$ by approximating the angle θ_0 at the screen as,

$$\theta_0 \approx \frac{\Delta\phi/k}{a} \approx \frac{e^2}{\pi m_e} \frac{\Delta n_e}{\sqrt{a}} \frac{\sqrt{D}}{f^2}, \tag{2.18}$$

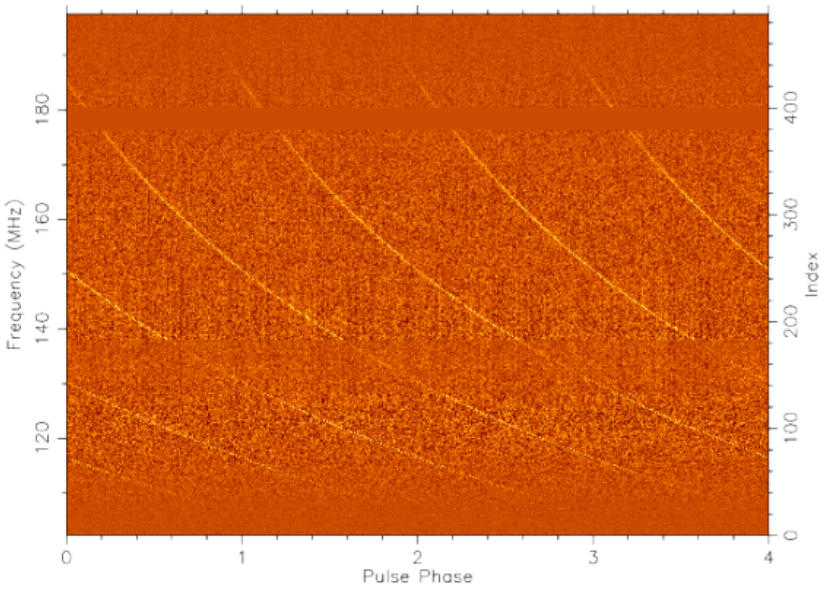

FIGURE 2.7: The ISM dispersion effects on the received pulses from PSR J1840+5640. As the radio waves from the source propagate through the interstellar medium, they interact with ionised-gas and their arrival times are delayed (dispersive delay). This delay depends on the observed frequency, as a result, the pulses at high frequency arrive earlier than those at the low frequency (image taken from Donner, 2017).

where $k = (2\pi/c)nf$, n is the refractive index (see Equation (2.9)) and d is the distance to the pulsar.

This leads to an observer seeing both, the angular radius θ_d of the diffuse scatter disk around the source,

$$\theta_d = \frac{\theta_0}{2} \approx \frac{e^2}{2\pi m_e} \frac{\Delta n_e}{\sqrt{a}} \frac{\sqrt{d}}{f^2}, \tag{2.19}$$

and the intensity distribution which follows a Gaussian probability distribution,

$$I(\theta)d\theta \approx \exp(-\theta^2/\theta_d^2)2\pi\theta d\theta. \tag{2.20}$$

The received scattered-waves therefore, will travel an additional distance, due to the small change in direction (e.g. Figure 2.8), and thus the path length will also increase which eventually leads to a geometrical time delay $\Delta t(\theta)$,

$$\Delta t(\theta) = \frac{\theta^2 d}{c}. \tag{2.21}$$

This effect can be used to obtain the observed intensity I as a function of time as,

$$I(t) \approx \exp(-c\Delta t/(\theta_d^2 d)) \equiv e^{-\Delta t/\tau_s}, \tag{2.22}$$

where

$$\tau_s = \frac{\theta_d^2 d}{c} = \frac{e^4}{4\pi^2 m_e^2} \frac{\Delta n_e^2}{a} d^2 f^{-4}. \tag{2.23}$$

This causes the observed scattering tail with the exponential shape that appears on the received pulse signal.

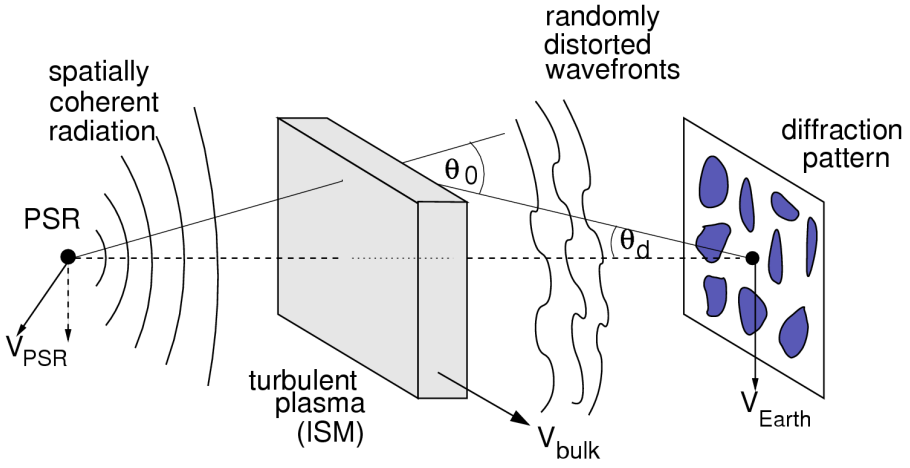

FIGURE 2.8: The observed scattering and scintillations effects (distorting of the waves from the pulsar by a thin screen of irregularities of various scales) due to inhomogeneities in the ISM. Figure taken from Handbook of Pulsar Astronomy by Lorimer and Kramer (2005).

2.4.3 Scintillation

Besides the dispersion and scattering of the ISM, an additional effect, called interstellar "scintillation" can also be observed. The scintillation is defined as a short-term intensity variation which appears in many pulsars. This is caused by the electron density variations between the pulsar and the observer.

Using a similar model as for the scattering, the thin screen model can be used for the analysis of the pulsar scintillation. Figure 2.8 shows that the scattered radiation from the pulsar to an observer leads to random irregularities of various scales. This phase difference will then be received along the line of sight by an observer as a scintillation pattern. Over a time scale τ_s, the received signals will show different phases (due to the

change in the intensity) as,

$$\delta\Phi \sim 2\pi f \tau_s. \tag{2.24}$$

The condition for interference to occur is when the phases of the waves do not differ by more than 1 radian. Therefore the scintillation bandwidth (Δf) can be described as follows,

$$2\pi \Delta f \tau_s \sim 1, \tag{2.25}$$

which gives a scaling of $\Delta f \propto 1/\tau_s \propto f^4$.
As the result, scintillation shows a pattern of intensity irregularities in both frequency and time, which can be measured by producing a two-dimensional image as a function of observed time and frequency called the *dynamic spectrum*. The regions of enhanced flux density in these dynamic spectra are referred to as *scintle*. The *scintle* size in frequency (scintillation bandwidth Δf) and time (scintillation timescale $\Delta\tau$) can be measured as the half-width at half-maximum of the auto-correlation function of the spectrum, and the half-width at $1/e$ along the time axis respectively.

In the case where the ionized gas in the ISM is modeled as a turbulent gas, the variation in electron density shows a distribution of scales, which is different from a single scale size, a, as presented above. By changing from the single size to a distribution of length scales which can be characterized by a spatial wavenumber spectrum, one can give a better interpretation for the observations. The extended power law model can be used as follows:

$$P_{n_e}(q) = \frac{C_{n_e}^2(z)}{(q^2 + k_0^2)^{\beta/2}} exp\left[-\frac{q^2}{4k_i^2}\right], \tag{2.26}$$

where $q = 1/a$ is the magnitude of the three-dimensional wavenumber, k_i and k_0 are the inner and the outer scales of the turbulence respectively, and $C_{n_e}^2(z)$ represents the strength of the fluctuations along the line of sight (for a full review on turbulence see Rickett, 1990). Integrating the term $C_{n_e}^2(z)$ along the line of sight gives the so-called *scattering measure* (SM) as,

$$SM = \int_0^d C_{n_e}^2(z) dz. \tag{2.27}$$

The scattering measure provides a measurement of the electron density fluctuations along the line-of-sight and can be identified from the broadening of the average pulse profile. In Equation (2.26), k_i and k_o are equal to the inner and outer cut-offs of scale sizes. As mentioned earlier, these scales describe the scales distribution of the electron density variations of the turbulent gas in the ISM. Considering wavenumber q between $k_o \ll q \ll k_i$, Equation (2.26) can then be re-written as a power law model with spectral index β as follows,

$$P_{n_e}(q) = C_{n_e}^2 q^{-\beta}. \tag{2.28}$$

For the turbulent media, one can apply a Kolmogorov spectrum with $\beta = 11/3$. This leads to frequency-dependence scattering time (τ_s) and decorrelation bandwidth (Δf_{DISS}) as follows,

$$\tau_s \propto f^{-\alpha}, \qquad \Delta f_{DISS} \propto f^{\alpha}, \tag{2.29}$$

where $\alpha = 2\beta/(\beta - 2)$, which gives $\alpha = 4.4$ for a Kolmogorov spectrum ($\beta = 11/3$) and $\alpha = 4$ for the thin screen model. The term Δf_{DISS} is referred to diffractive interstellar scintillation bandwidth. In Chapter 4, we will apply DM structure function analysis to the resulted DM variations from the observations, which enable us to examine either they show a compatible result with Kolmogorov spectrum or not.

2.5 Pulsar Timing

Pulsar timing is the measurement of a time-of-arrivals (TOAs) of pulses from the neutron stars. These TOAs are computed by fitting the so-called *timing model* (see § 2.5.3) to the observed time-of-arrival of pulses. As a result, the difference between the observed and predicted arrival times gives the so-called *timing residual*. Study and analysing of these residuals is considered the basis of all pulsar timing which can be obtained by searching for correlation in the signals of the pulsar timing residuals (Hobbs, 2009).

Pulsar timing applications are ranging from studying the ISM properties, the mass of the neutron stars, stellar evolution and searching for the stochastic gravitational waves (GWs) background. Similarly, applying pulsar timing techniques on pulsars in a binary system enables measurements of their orbits, rotation slowdown and testing Einstein's theory of General Relativity (GR).

Multiple efforts were started to construct pulsar Timing Arrays to perform high-precision pulsar timing using pulsar observations over a long time duration. These are three sub-individual projects which are: European Pulsar Array (EPTA) in Europe, Parkes Pulsar Timing Array (PPTA) in Australia and North American Nanohertz Observatory for Gravitational Waves (NANOGrav) in the United States. As the main aim of PTAs is to deliver a direct detection of the stochastic gravitational waves background, the data from the three PTAs projects are being combined in the so-called International Pulsar Timing Array (IPTA, e.g Hobbs et al., 2010, Verbiest et al., 2016).
The current and near future of pulsar timing is very promising. This is thanks to the new instruments such as FAST telescope in China and MeerKAT in South Africa which has been launched on Friday the 13th of July 2018. One of MeerKAT key science programs in pulsar timing is MeerTIME (Bailes et al., 2018), which aims to observe over 1000 pulsars, during the period of five years, with the MeerKAT telescope in an efforts to detect the stochastic gravitational waves (GW) background, study the interiors of neutron stars, tests the relativistic theory of gravity and other topics related with pulsar science.

In this section, an overview of pulsar timing techniques, TOAs and timing model and its parameters are given. This section is based on Lorimer and Kramer (2005) and the recent review by Manchester (2017).

2.5.1 Time of Arrivals (TOAs)

The time of arrival (TOA) is defined as "the arrival time of the nearest pulse to the mid-point of the observation" Lorimer and Kramer (2005). In pulsar timing, the TOAs taken from pulsars observations over long interval enable us to create a timing model; which then can be used to determine the parameters of the pulsars, with a good accuracy, and perform the analyses of their evolution. Practically, to measure the arrival times of the pulses, the pulsars data need to be folded at the period of the pulsar. As a result, the so-called "*average pulse profile*" will be created.

2.5.2 Template Matching

The cross-correlation method is considered the best method for measuring the timing of arrival of pulsars (see Taylor, 1992). In this method, the observed profile is matched with a high signal to noise (S/N) template. In our case, this template is constructed from a set of earlier observations at a known range of frequencies.
By considering a scaled and shifted template $\mathcal{T}(t)$ with added noise $\mathcal{N}(t)$, the average pulse profile $\mathcal{P}(t)$ then can be written as,

$$\mathcal{P}(t) = a + b\mathcal{T}(t - \tau) + \mathcal{N}(t), \tag{2.30}$$

where a is the arbitrary offset, b is scaling factor and τ is the phase offset which shows the time-shifted between the template and the profile. By applying the cross-correlation between templates and the data (either in time domain or frequency domain), TOAs can be measured.

The measurements of the TOAs can be done with high precision however, many effects, either associated with the pulsars or as systematic effects, can limit it. This introduces an uncertainty in the measurements of TOAs which can be calculated by the following formula,

$$\sigma_{TOA} \simeq \frac{S_{sys}}{\sqrt{t_{obs}\Delta f}} \times \frac{P\delta^{3/2}}{S_{mean}}. \tag{2.31}$$

Where S_{sys} is the flux density of the system, Δf is the observed bandwidth, P is the pulse period, t_{obs} is the integration time, $\delta = W/P$ is the pulse duty cycle and the mean flux density is given by S_{mean} (Lorimer and Kramer, 2005).

2.5.3 Pulsar Timing-Model Parameters

In pulsar timing, the measured TOAs from the received pulses at the observatory need to be fitted to a model by using an appropriate method (e.g cross-correlation 2.5.2). Considering this fitting, there will be variations between the TOAs at the telescope and the time of emission at the pulsar; hence, a timing model is required to correct all the effects which limit our ability to measure the average TOAs with high accuracy.

Here some of the parameters of the timing model and how they appear in the timing residuals of the observations are discussed (e.g. Figure 2.9). For the full review see Edwards et al. (2006).

- Barycentric corrections
  Observatories on Earth measure the pulse TOAs by an atomic time standard called "Terrestrial Time (TT)"; Measuring the TOAs using the observatory clock known as "topocentric arrival time" which occurs in a non-inertial frame, due to rotating Earth orbiting the Sun. Therefore, one needs to transfer this to an inertial reference frame which represents the center of mass for the solar system. The frame of Solar system barycenter (SSB) is approximated as a perfect inertial frame to measure

the TOAs "barycentric arrival time".

The transformation from the topocentric TOA to barycentric TOAs is given by

$$t_{SSB} = t_{topo} + t_{corr} - \Delta D/f^2 + \Delta_{R_\odot} + \Delta_{S_\odot} + \Delta_{E_\odot}. \tag{2.32}$$

Equation (2.32) can be used as a reference to explain each term as follows:

- Clock corrections

  The first two terms in Equation (2.32) t_{topo} and t_{corr} are corresponding to the time measured by the observatory clock (topocentric time) and the observatory clock corrections, respectively.

- Frequency corrections

  $\Delta D/f^2$ represents the dispersion measure and dispersion constant corrections. As we showed in § 2.4.1 the pulses traveling through the ISM are delayed due to the interaction with the ISM (dispersive delay), which shows that the TOAs depend on the observed frequency (f).

- Romer delay

  The term $\Delta_{R_\odot}$ denotes the vacuum delay between the arrival of the pulse at the observatory and SSB frame and can be given as,

$$\Delta_{R_\odot} = -\frac{\overrightarrow{r}.\hat{s}}{c}, \tag{2.33}$$

  where $\overrightarrow{r}$ is a vector pointing from the SSB frame toward the observatory, and more precisely, can be divided to two components, $\overrightarrow{r}_{SSB}$ which connect the SSB with the center of the Earth (geo-centre) and $\overrightarrow{r}_{EO}$ which connect the geo-center with the phase center of the telescope. The second vector $\hat{\mathbf{s}}$ in Equation (2.33) is pointing from the SSB frame to the position of the pulsar.

- Shapiro delay

  The Shapiro delay $\Delta_{S_\odot}$ is a time delay of the pulses due to the curvature of space-time. The total of this delay can be measured by adding all the masses in the solar system as,

$$\Delta_{S_\odot} = -2\sum_i \frac{GM_i}{c^3} ln\left[\frac{\hat{s}.\overrightarrow{r}_i^E + r_i^E}{\hat{s}.\overrightarrow{r}_i^P + r_i^P}\right], \tag{2.34}$$

  where G is Newton gravitational constant, M_i is the mass of the included body i, $\overrightarrow{r}_i^P$ and $\overrightarrow{r}_i^E$ are pulsar position and telescope position relative to the body i respectively.

  Note that, since the Sun and Jupiter have the largest Shapiro delay in the solar

system ($\sim 120\ \mu s$ and $\sim 200\ ns$, respectively), only the Sun, and sometime Jupiter, is taken into account when calculating the Shapiro delay in the Solar System.

- Einstein delay

  The Einstein delay is the combined effect of time dilation due to both; the Earth motion (change the distance between the observatory and the pulsar, or the orbital period) and the gravitational red-shift caused by the masses of the bodies in the solar system, and given as,

$$\Delta_E = \gamma sinE, \tag{2.35}$$

  which shows a sinusoidal shape in the residual. Where in binary systems (PK parameters) γ referred to amplitude measured in seconds, and it's given as,

$$\gamma = T_{\odot}^{2/3} \left(\frac{P_b}{2\pi}\right)^{1/3} e \frac{m_2(m_1 + 2m_2)}{(m_1 + m_2)^{4/3}}, \tag{2.36}$$

  where e is the eccentricity.

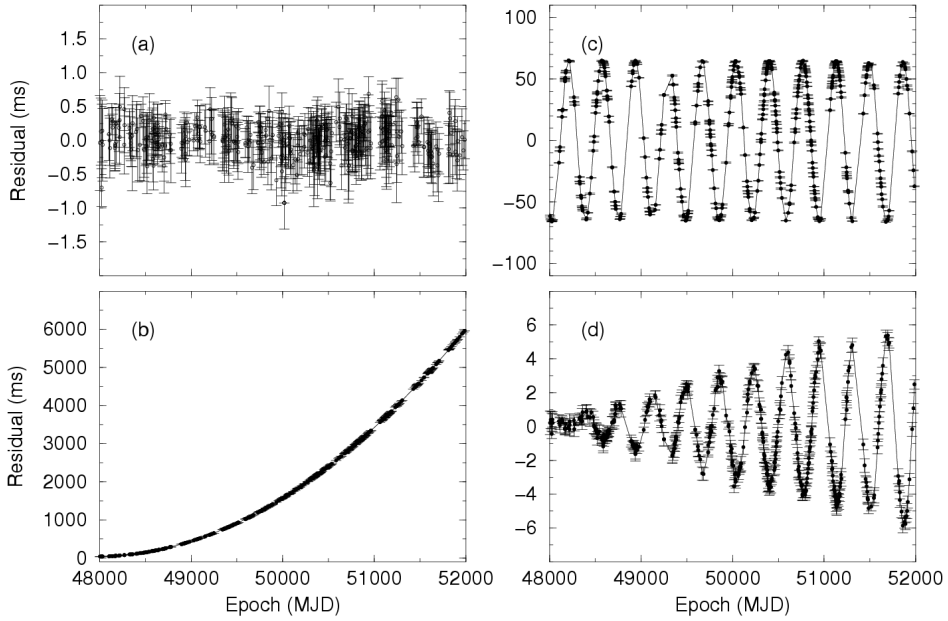

FIGURE 2.9: Timing-model parameters and their effects on the residual structure. Panel (a) shows an accurate timing model in which all the residual centered around 0 ms. Panel (b) The spin down (or frequency derivative) errors which give a linearly increase shape. Panel (c) The position error which gives a sinusoidal shape due to the variation with the period of the Earth around the sun (1 year). Panel (d) shows inaccurate pulsar's proper motion measurements which result in 1-year sinusoid shape with linearly-increasing amplitude (Lorimer and Kramer, 2005).

Chapter 3

Observations and Data Reduction

The data used in this thesis were collected with the LOw-Frequency ARray (LOFAR) telescope. Specifically, the observations were performed with international LOFAR stations: the Nançay station (FR606) in France, the Onsala station (SE607) in Sweden and stations in Germany (DE601 - Effelsberg, DE602 - Unterweilenbach, DE603 - Tautenburg, DE605 - Julich). In this chapter, a general overview of the LOFAR telescope is given in § 3.1 and a full description of the observations used in this study are given in § 3.2. In § 3.3 the data reduction process is explained.

3.1 LOw Frequency ARray (LOFAR)

The LOw-Frequency ARray (LOFAR, van Haarlem et al., 2013) is a unique radio telescope that contains a number of interferometric arrays of dipole antenna stations spread throughout Europe. LOFAR was designed and developed by the Netherlands Institute for Radio Astronomy (ASTRON)[1]. It operates within the low-frequency regime of the radio wavelengths, which is divided into low band (10 - 90 MHz) and high band (110 - 240 MHz). The range of these frequencies corresponds to wavelengths between 30 and 1.2 m. Additionally, LOFAR has a large field-of-view (FoV), which makes it an excellent instrument for many key science projects such as surveying the low-frequency sky, the transient radio sky and conducting pulsar studies and surveys. More details about the pulsar key science projects are described in Stappers et al. (2011).

LOFAR telescope comprises of 38 stations in the Netherlands and thirteen international stations distributed within the European partner countries (e.g. Figure 3.1). The international stations are located in France, Germany, Ireland, Poland, Sweden and the

[1] https://www.astron.nl/

United Kingdom. Recently, Austria,Ukraine and Italy have joined the International LOFAR Telescope (ITL[2]) with intentions to construct their own LOFAR stations. In Finland, the Kilpisjärvi Atmospheric Imaging Receiver Array (KAIRA) makes use of LOFAR antennas and digital signal-processing hardware but operates it as a stand-alone instrument (McKay-Bukowski et al. 2015).

Similar to the individual antennas in interferometric radio telescopes such as MeerKAT and the VLA, LOFAR stations can also perform the same basic functions e.g. tracking sources by combining the signals from individual antenna elements to form the so-called *phased array*. Figure 3.1, (A) shows the geographical distribution of existing constructed LOFAR station across Europe, whereas in (B) the distribution of high-band-antennas (HBAs) and low-band-antennas (LBAs) within a station is shown.

LOFAR stations are classified based on their size and role, to three types as follows:

- **Core Stations**: Located in the Netherlands next to Exloo, a town in the north-eastern Dutch province of Drenthe, and consists of 24 stations distributed within a radius of 2 km. The central region of LOFAR is known as the "Superterp" and contains six stations within a diameter of 320 m. These Superterp stations provide the shortest baselines in the array. Each station in the core comprises of 96 Low Band Antennas (LBAs) and 48 High Band Antennas (HBAs). Figure 3.2 shows the central part of the core as well as a number of additional core stations around it.

- **Remote Stations**: These 14 stations are distributed on an approximately logarithmic spiral over a radius of 90 km. Both the core and remote stations are distributed over a diameter of 180 km. Remote stations also contain 96 LBAs and 48 HBAs.

- **International LOFAR Stations**: Currently, there are 13 functional international stations distributed throughout Europe (Figure 3.1, B). Each of these stations has 96 LBAs and 96 HBAs. These stations are located in the following countries:

  – France - Nançay. LOFAR Super Station (LSS) under construction, also known as New extension in Nançay upgrading LOFAR (NenuFAR), which will add 96 low-frequency mini-arrays to the current Nançay station (FR606). Each of these mini-arrays consists of 19 dipole antennas to give a total of $96 \times 19 = 1824$ dual-polarized antennas. NenuFAR will cover the frequency range of LOFAR-LBA and extend it to lower ranges between 10 MHz and 85 MHz (e.g. Zarka et al., 2015), thanks to more sensitive antennas.

[2] http://www.astron.nl/lofar-crosses-alps-italy-joins

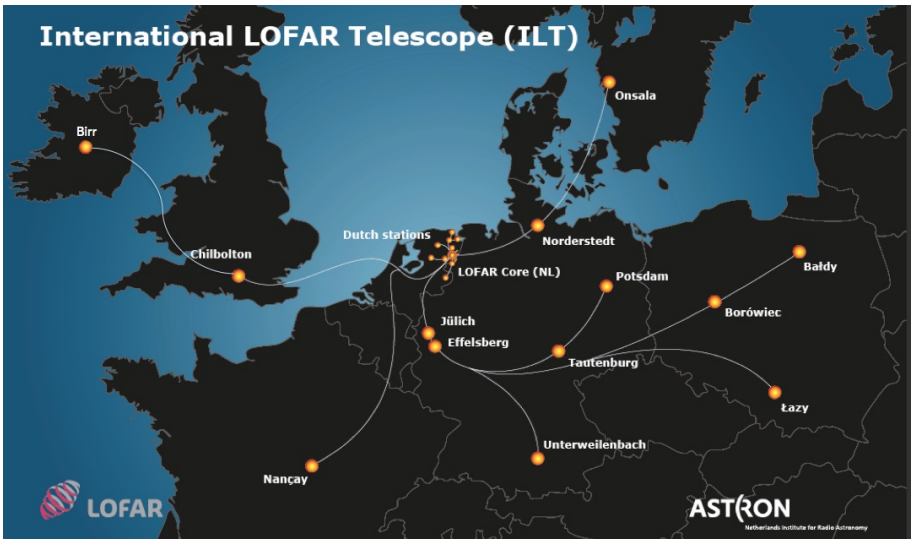

(A)

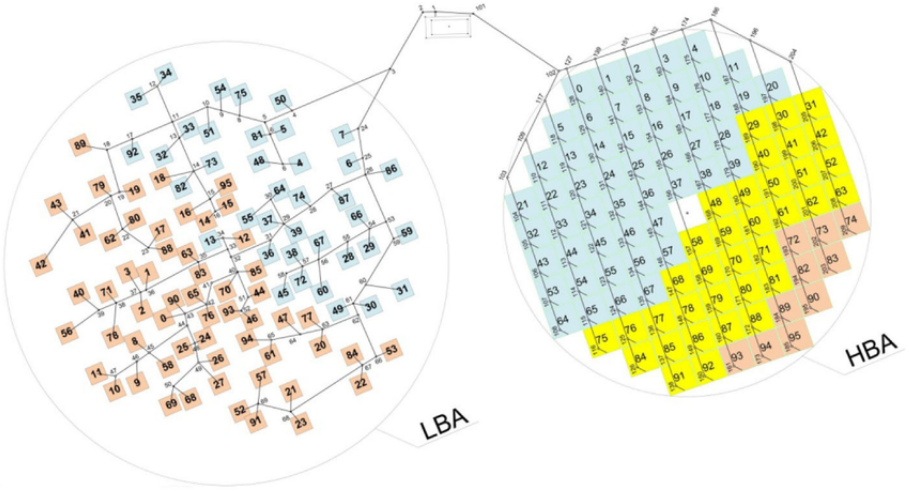

(B)

FIGURE 3.1: Panel (A): the current distribution of LOFAR stations within Europe (Image credit: https://www.astron.nl/node/1405). Panel (B): the layout diagram of the typical international LOFAR stations include the LBA antennas and the HBA tiles (Dabrowski et al., 2016).

- Germany - Effelsberg, Garching, Potsdam, Tautenburg, Julich, Norderstedt.
- United Kingdom - Chilbolton.
- Sweden - Onsala.
- Poland - Baldy, Borowiec, Lazy.
- Ireland[3] - One station completed in July 2017, Birr.
- Latvia - One station under construction.
- Italy - recently has joined the International LOFAR Telescope (ITL).
- Finland - One prototype-station funded and completed, Kilpisjärvi.

[3] http://lofar.ie/i-lofar/

(A) Superterp

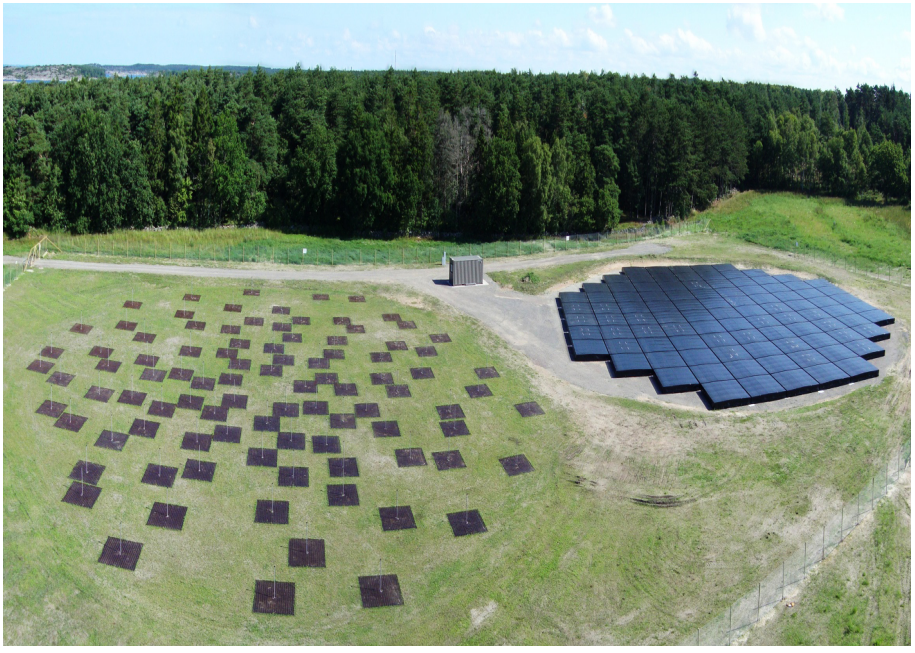

(B) SE607 Station

FIGURE 3.2: (A) Aerial view of part of LOFAR with the Superterp in the middle (van Haarlem et al., 2013). (B) The image of Swedish LOFAR station in Onsala Space Observatory. The LBA antennas are located at the left side of the photo, while HBA tiles are clustered together in the right side. The station digital back-end (contains the digital receiver units (RCUs), digital signal processing (DSP), local control unit (LCU), remote station processing (RSP)) are located in the container visible in the top center of the photo. Credit: Onsala Space Observatory/Leif Helldner.

All LOFAR stations consist of two types of antennas described below:

- **Low-Band Antenna (LBA)**
  The low-band antenna covers a frequency range between 10 MHz and 90 MHz. It consists of dipole elements, each of which has a length of 1.38 m and is sensitive to two orthogonal linear polarizations. There are 96 low-band antenna elements in an international station, which are used as a single antenna array. Both, the core and remote stations consist of 98 LBAs arranged in a single 87 m diameter field.

- **High Band Antenna (HBA)**
  The high-band antenna covers a frequency range from 110 MHz to 240 MHz. 16 HBAs antenna elements (dual polarized) are clustered and phased to create a single tile. Each of these tiles contains an analogue beamformer and low-noise amplifier able to create a single "*tile beam*" for any given direction in the sky. The number and distribution of HBA tiles are different in the three types of LOFAR stations. While the international station consists of a single array of 96 tiles, remote station consists of 48 HBAs arranged in a single 41 m diameter and the core station consists of 48 HBAs arranged in two 24-elements fields where each field has a diameter of 30.8 m.

Signal processing with LOFAR

Each LOFAR station has a cabinet that contains receiver units (RCUs), digital signal processing (DSP) boards, a local control unit (LCU), and other additional equipment which are used to process the signals at the early stages. A brief description of data processing in LOFAR can be given as follows: after receiving the signals at the LBA elements or HBA tiles, they are transferred to the RCUs via coaxial cables. The RCUs performs filtering, amplification, conversion to base-band frequencies and digitization of the input signal. Subsequently, the received signals enter the remote station processing boards (RSPs) for all the digital signal processing. In the RSPs, the signals are first buffered to remove the differences in signal delays in the coaxial cables. Then, the signals are filtered into 512 sub-bands by a polyphase filter. Based on the sample clock frequency, the sub-bandwidth can be 195.312 kHz (200 MHz clock) or 156.250 kHz (160 MHz clock). The station beam is produced by RSP boards and the resulting product is divided into four separate *lanes*. These lanes are then streamed to either a local processing backend or to the central processor (CEP) in Groningen.

In addition to a RCU and DSP, as mentioned before each LOFAR station contains a local control unit (LCU). This unit consists of a server computer running a Linux operating system, which is used to control the station. Additionally, LCU receives clock signals from the Global Positioning System (GPS) and a rubidium standard.

3.2 Observations

The observations used in this thesis are part of a long-term running observing proposal (LC0 - 014, LC1 - 048, LC2 - 011, LC3 - 029, LC4 - 025, LT5 - 001, LC9 - 039 and LT10 - 014, PI: Serylak) that aims to observe known pulsars with international LOFAR stations, monitoring them with a weekly cadence where each observing session lasts approximately one hour per target. A total number of 95 sources were selected and monitored, this includes 14 millisecond pulsars and 81 slow pulsars, 5 of which were discovered as part of the LOFAR Tied-Array All-Sky Survey[4] (LOTAAS, Coenen et al., 2014).

In this thesis, 27 sources from the running observing proposal were not included, due to e.g. insufficient signal to noise ratio (SNR) or the number of observations, excluding all the millisecond pulsars, which reduced the total number of used sources to 68. This includes only slow pulsars and 3 of the LOTAAS and LOFAR Tied-Array Survey[5] (LOTAS, Coenen et al., 2014) discovered sources. In the analysis stage, observations in the period roughly between June 2014 and November 2017 were used. Each observation was performed for at least one hour (except PSR J0332+5434 which has 30 minutes observations) but not longer than two hours, in order for a pulsar to achieve the required SNR.

All the observations were taken with HBAs, in the frequency range between 110 to 190 MHz. The data were recorded by LOFAR and MPIfR Pulsare (LuMP) Software[6]. This software is used for recording beamformed data from a LOFAR station in the single-station mode. All the data in this study are coherently dedispersed to remove the possible dispersion smearing within specific frequency channels. In the following sub-sections, I give an overview of the international LOFAR stations which are used to obtain the data.

3.2.1 Observations with French Station (FR606)

The total number of pulsars observed with FR606 and used in this analysis is 21, details of which are listed in Table (3.1). This number includes PSR J0613+3731, a source discovered by LOTAS. The full bandwidth of observations from FR606 is 95.31 MHz with a centre frequency of 149.9 MHz. This bandwidth was then split into 4 *lanes* with central frequencies of 114.16 MHz, 137.98 MHz, 161.81 MHz and 185.64 MHz for each frequency band consequently. During the observation, the data were recorded by 4 local

[4] http://www.astron.nl/lotaas/index.php?sort=0&order=0
[5] http://www.astron.nl/pulsars/lofar/surveys/lotas/
[6] https://github.com/AHorneffer/lump-lofar-und-mpifr-pulsare

TABLE 3.1: The initial parameters for the total number of pulsars from FR606. These parameters are PSR B (based on B1950 designation), PSR J (based on J2000 designation), pulse period (P), dispersion measure value (DM). The table is obtained using Australia Telescope National Facility (ATNF) Pulsar Catalog (Manchester et al., 2005).

#	PSR B	PSR J	Pulse Period(s)	DM ($cm^{-3}pc$)
1	B0138+59	J0141+6009	1.222	34.926
2	B0320+39	J0323+3944	3.032	26.189
3	B0329+54	J0332+5434	0.714	26.764
4	B0450+55	J0454+5543	0.340	14.590
5	B0540+23	J0543+2329	0.245	77.702
6	-	J0613+3731**	0.619	18.990
7	B0809+74	J0814+7429	1.292	5.750
8	B0834+06	J0837+0610	1.273	12.864
9	B0950+08	J0953+0755	0.253	2.969
10	B1133+16	J1136+1551	1.187	4.840
11	B1237+25	J1239+2453	1.382	9.251
12	B1508+55	J1509+5531	0.739	19.619
13	B1540−06	J1543−0620	0.709	18.377
14	B1642−03	J1645−0317	0.387	35.755
15	B1737+13	J1740+1311	0.803	48.668
16	B1822−09	J1825−0935	0.769	19.383
17	B1931+24	J1933+2421	0.813	106.03
18	B2016+28	J2018+2839	0.557	14.197
19	B2111+46	J2113+4644	1.014	141.26
20	B2224+65	J2225+6535	0.682	36.443
21	B2310+42	J2313+4253	0.349	17.276

** LOTAS discovery

backends, to a large volume storage. All the observations with less than four parts of the frequency bands were excluded from the study.

3.2.2 Observations with Swedish Station (SE607)

The Swedish LOFAR station[7] is located at Onsala Space Observatory. The configuration of this station is identical to that of the French Station (FR606). A total of 13 pulsars from the SE607 station was used in this study. Table (3.2) displays all pulsars observed with the station including the LOTAAS discovered pulsar, PSR J0815+4611. These observations have the same properties as the data from FR606 (e.g. central-frequency, number of channels, bandwidth etc.) and therefore, a similar approach was used during data reduction steps (see § 3.3).

[7] http://www.chalmers.se/en/researchinfrastructure/oso/radio-astronomy/lofar/Pages/default.aspx

TABLE 3.2: The initial parameters for the total number of pulsars from SE607. These parameters are PSR B (based on B1950 designation), PSR J (based on J2000 designation), pulse period (P), dispersion measure value (DM). All the samples were obtained using Australia Telescope National Facility (ATNF) Pulsar Catalog (Manchester et al., 2005) except J0815+4611 which is LOTAAS discovery and its parameters were obtained from the initial ephemeris.

#	PSR B	PSR J	Pulse Period(s)	DM ($cm^{-3}pc$)
1	-	J0051+0423	0.354	13.9
2	B0059+65	J0102+6537	1.679	65.853
3	B0331+45	J0335+4555	0.269	47.145
4	-	J0540+3207	0.524	61.97
5	-	J0546+2441	2.843	73.81
6	B0655+64	J0700+6418	0.195	8.773
7	-	J0815+4611**	0.434	11.27
8	B0917+63	J0921+6254	1.567	13.154
9	B1112+50	J1115+5030	1.656	9.186
10	B1322+83	J1321+8323	0.67	13.316
11	B1839+56	J1840+5640	1.652	26.771
12	B1953+50	J1955+5059	0.518	31.982
13	B2319+60	J2321+6024	2.256	94.591

** LOTAAS discovery

3.2.3 Observations with the LOFAR Stations in Germany

As mentioned earlier, there are 6 international stations located in Germany and operated by the German LOng Wavelength (GLOW)[8] group, which is a consortium formed by a number of German universities and research institutes.

A set of 34 sources was obtained from four stations, namely DE601, DE602, DE603 and DE605. As opposed to the sources observed by FR606 or SE607, each source was observed with more than one German station throughout 3.5 years of monitoring. Table (3.3) shows all the data obtained from LOFAR stations in Germany.

The observations made with German stations have relatively longer observation spans due to sources with weaker SNRs. Two sets of German station data were used which include: i) early observations starting from mid August 2013 which have a total bandwidth of 95.31 MHz and centre frequency 149.9 MHz. Each observation, using the full bandwidth, was divided into four *lanes*, where each lane has 122 frequency channels, 1024 number of pulse phase bins and a lane width of 23.828 MHz. ii) later observations which started in February 2015. In order to reduce the data rate for all German stations

[8] https://www.glowconsortium.de/index.php/en/

(except DE601 which consists of 4 lanes), the outer parts of the band, where the instrumental sensitivity is very low, were removed and as a result, the total bandwidth was reduced to 71.484 MHz with a centre frequency of 153.808 MHz. The full bandwidth was then divided into three *lanes* with 122 frequency channels, 1024 number of pulse phase bin, and center frequency of 23.828 MHz for each. Additionally, the observations with large differences in their number of the sub-integrations were rejected from the reduction.

3.3 Data Reduction

Data reduction was performed using the readily available pulsar reduction package PSRCHIVE[9] (Hotan et al., 2004). In order to manage the reduction, PYTHON scripts were prepared to operate the required tasks. These include updating the ephemeris and performing radio frequency interference (RFI) excision. Additionally, BASH scripts were also prepared and used to perform tasks such as, creating diagnostic plots and producing final reports summarizing the reduction process. With the intention to decrease the processing time, the data reduction was parallelized. This, in turn, allowed to complete the data reduction in the shortest possible time (See Figure 3.3).

3.3.1 Data Processing

The first step of data reduction involved sorting the observations based on a number of frequency channels and number of sub-integrations. Then, all the archives for each observation were added to form a single file covering the bandwidth (488 frequency channels for FR606 and SE607 and 366 frequency channels for the German stations).

In the following step, the resulting files were adjusted by removing edges of the band where antennas were not sensitive. This was implemented by removing the first 39 and last 49 frequency channels creating an archive file with 400 frequency channels. This procedure was performed for all observations taken with the FR606 and SE607 stations, as well as early observations performed with the German stations. No channel removal was applied for the recent observations with German stations (three lanes) and therefore, the number of the frequency channels was kept to be 366. At this stage, the ephemeris of the archives were checked for uniformity and updated to a common version if discrepancies were found.

As mentioned earlier, all observations were taken within the low-frequency band of HBA antenna and close to the FM band (ranging between 87.5 MHz and 108 MHz) and

[9] http://psrchive.sourceforge.net/

TABLE 3.3: The initial parameters for the total number of pulsars from LOFAR Stations in Germany. These parameters are PSR B (based on B1950 designation), PSR J (based on J2000 designation), pulse period (P), dispersion measure value (DM). These parameters were obtained using Australia Telescope National Facility (ATNF) Pulsar catalog (Manchester et al., 2005).

#	PSR B	PSR J	Pulse Period(s)	DM $cm^{-3}pc$
1	B0052+51	J0055+5117	2.115	44.012
2	B0105+65	J0108+6608	1.283	30.548
3	B0136+57	J0139+5814	0.272	73.811
4	B0301+19	J0304+1932	1.387	15.656
5	B0339+53	J0343+5312	1.934	67.30
6	B0355+54	J0358+5413	0.156	57.142
7	B0402+61	J0406+6138	0.594	65.405
8	B0450−18	J0452−1759	0.548	39.903
9	B0525+21	J0528+2200	3.745	50.869
10	B0611+22	J0614+2229	0.334	96.91
11	B0626+24	J0629+2415	0.476	84.176
12	B0818−13	J0820−1350	1.238	40.938
13	B0820+02	J0823+0159	0.864	23.727
14	B0823+26	J0826+2637	0.530	19.476
15	B0919+06	J0922+0638	0.430	27.298
16	B0943+10	J0946+0951	1.097	15.318
17	B1540−06	J1543−0620	0.709	18.377
18	-	J1740+27**	1.058	35.50
19	B1749−28	J1752−2806	0.562	50.372
20	B1818−04	J1820−0427	0.598	84.435
21	B1831−04	J1834−0426	0.290	79.308
22	B1857−26	J1900−2600	0.612	37.994
23	B1911−04	J1913−0440	0.825	89.385
24	B1919+21	J1921+2153	1.337	12.443
25	B1929+10	J1932+1059	0.226	3.183
26	B1933+16	J1935+1616	0.358	158.521
27	B1940−12	J1943−1237	0.972	28.918
28	B1946+35	J1948+3540	0.717	129.367
29	B2020+28	J2022+2854	0.343	24.631
30	B2021+51	J2022+5154	0.529	22.549
31	B2045−16	J2048−1616	1.961	11.456
32	B2154+40	J2157+4017	1.525	71.123
33	B2217+47	J2219+4754	0.538	43.497
34	B2255+58	J2257+5909	0.368	151.082

** LOTAAS discovery

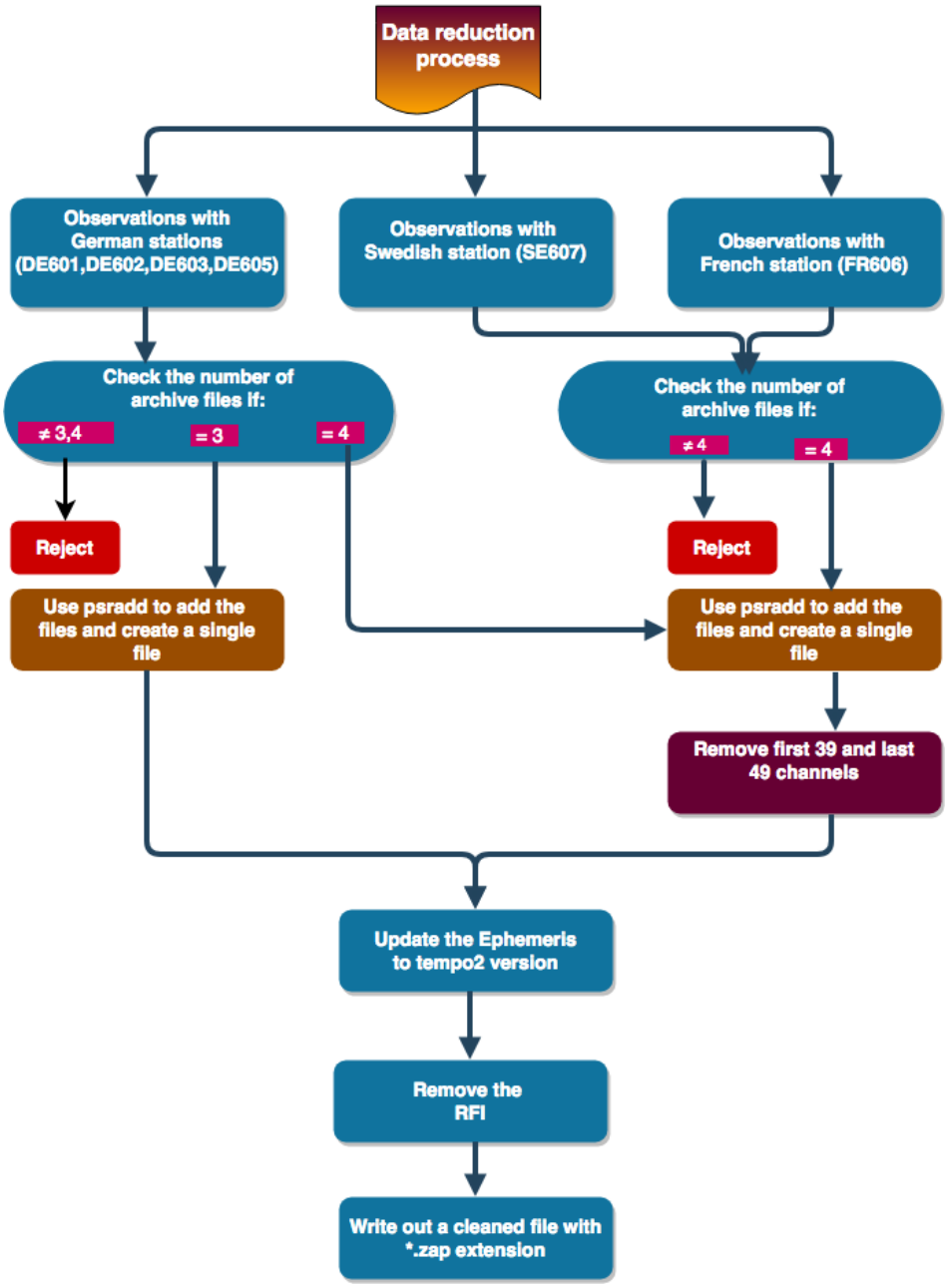

FIGURE 3.3: A diagram presenting the processes of the data reduction performed in this thesis.

other man-made RFI. As a result, RFI significantly impacted pulsar observations and timing precision and therefore had to be removed from observations. An example of an observation not corrupted by RFI for PSR J0828+2637 is given in Figure 3.4, while in the next (e.g. Figure 3.5), an observations of the same source even after an extensive FRI cleaning (40% of the data flagged) had to be removed from the analysis.

At this stage of the processing, the RFI excision was performed for all the observations

included in the study by using SURGICAL cleaner which is part of the COASTGUARD[10] tool (Lazarus et al., 2016). Implementing aforementioned cleaning strategy on all observations allowed me to identify and remove those parts of the data corrupted by the RFI. COASTGUARD has a set of parameters and settings which can be adjusted if the initial processing does not give a satisfactory result.

In this study, I faced many challenges associated with RFI impacting the quality of the data. In order to asses the quality of the reduced data, I prepared a diagnostic report to inspect each observation (e.g. Figure 3.4). It contains numerical values such as the amount of RFI removed from an observation, observational parameters, SNR etc. The report also contains a number of diagnostic plots for visual inspection i.e. a sub-integration stack, average profile, frequency profile, dynamic spectrum, and bandpass. The average number of observations is roughly 160 per pulsar, where an average of 28 observations were rejected due to many reasons e.g. RFI, insufficient bandwidth etc.

[10] https://github.com/plazar/coast_guard

Parameter	Description
STEM	J0826+2637_57157.6124982
NAME	J0826+2637
NBIN	1024
NPOL	1
NCHAN	366
NSUBINT	780
TYPE	Pulsar
LENGTH	7799.69297407996 (s)
SITE	DE603
RM	0 (rad/m^2)
DM	19.4540004730225 (pc/cm^3)
S/N	1656.76879882812
FREQ	153.80859375 (MHz)
BW	71.484375 (MHz)
COORD	08:26:51.383+26:37:23.79
% RFI	20.47218719349866890800

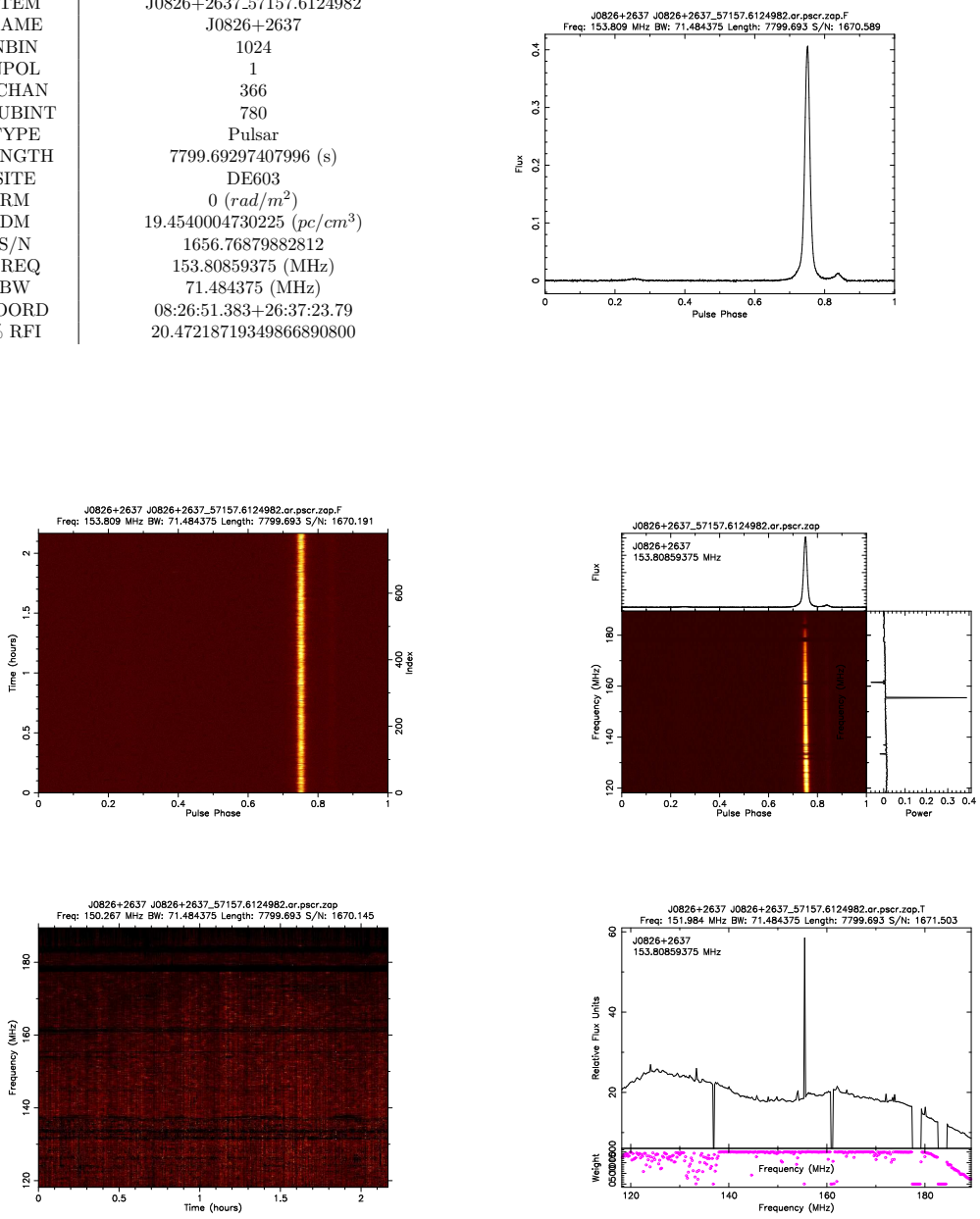

FIGURE 3.4: Example of a diagnostic report for PSR J0828+2637. Each panel is showing different type of information: average profile (top-right), sub-integration stacks (center-left), frequency resolved average profile (center-right), dynamic spectrum (bottom-left) and bandpass (bottom-right).

Parameter	Description
STEM	J0826+2637_56772.6986083
NAME	J0826+2637
NBIN	1024
NPOL	1
NCHAN	400
NSUBINT	168
TYPE	Pulsar
LENGTH	1679.95838976 (s)
SITE	DE605
RM	0 (rad/m^2)
DM	19.4540004730225 (pc/cm^3)
S/N	90.9390487670898
FREQ	148.92578125 (MHz)
BW	78.125 (MHz)
COORD	08:26:51.383+26:37:23.79
% RFI	40.63244047619047619000

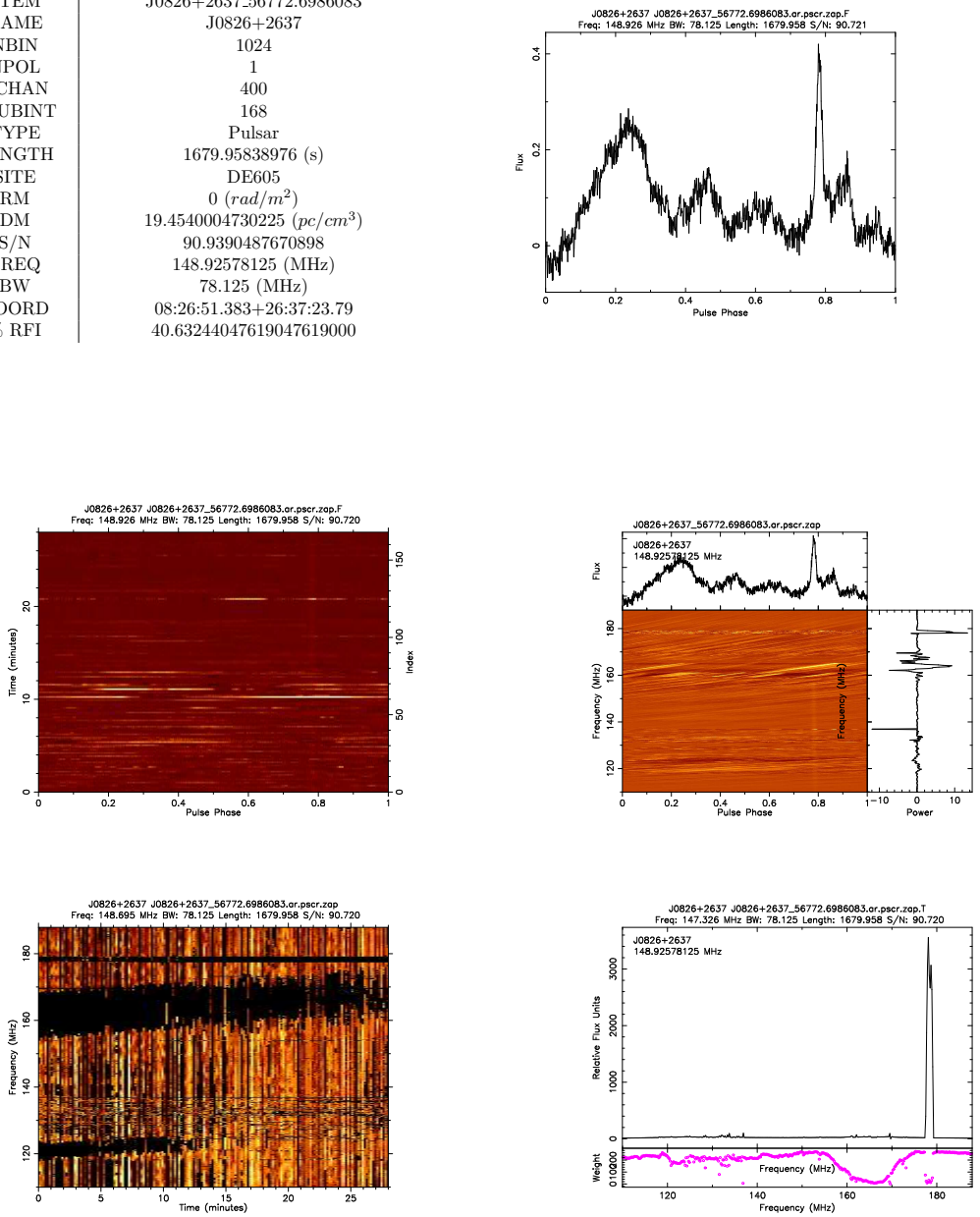

FIGURE 3.5: Example of an intensive RFI impacting an observation of PSR J0828+2637. The RFI of 40% reduced the S/N of the observation, and its effects can be seen in all of the diagnostic plots. Due to the severity of the interference this observation was removed from further analysis.

Chapter 4

Data Analysis and Results

The analysis of this study was performed with PSRCHIVE pulsars analysis package tool (Hotan et al., 2004) and TEMPO2 pulsar timing analysis software package (Hobbs et al., 2006). I also used PYTHON and BASH scripts to maintain the analysis processes, produce different plots and perform pulsar timing analysis. This chapter is divided into two main sections, data analysis (§ 4.1) where I show the analysis procedure e.g. improving standard profiles, pulsar timing, DM structure function. In the second section (§ 4.2), I present the results of the study which includes the dispersion measure variations, the new ephemeris for LOTAS/LOTAAS discovered pulsars and the influence of the solar position on the DM measurements.

4.1 Data Analysis

The analysis was performed for each pulsar in the data set, with the aim of obtaining the DM measurements.

4.1.1 Timing and DM Measurements

The main objective of this part is to improve the initial timing model (i.e. ephemeris file) for each pulsar in the data set. An updated timing model is very important to obtain a precise DM measurement and improve other pulsar parameters e.g. period, period derivative, position and proper motion. To achieve this goal, I prepared a BASH script that makes use of two PYTHON scripts MAKE_TEMPLATES.PY and MAKE_TOAS.PY which were written by Lucas Guillemot (LPC2E/Orleans; private communication, 2018). The analysis of this part was carried through two stages as follows:

First Iteration

In this iteration, the RFI cleaned data was sub-divided to a number of sub-integrations and sub-bands to check and improve the initial ephemeris of the data. Next, these data were used to generate the first standard template and TOAs. Subsequently, TEMPO2 was used to obtain the timing residuals.

- **The Standard Template Profile**
  This is the a typical profile for pulsar observations which is used to determine their TOAs. In order to create a standard template from the reduced data, full-intensity average profiles were created and averaged in time and frequency. Then, the SNR was determined for each of these averaged profiles. Subsequently, a single template was created, from all the observations of a specific pulsar, by adding the top 10 profiles with the highest SNR. The summation of these profiles was done by using PSRADD tool, where at this stage, the phase alignment between the added profiles was applied by including the -P flag of the PSRADD tool. This stage was illustrated in Figure 4.1, where panel (A) shows no alignment between the added profile and panel (B) shows the profiles after the alignment was applied. Next, the PSRSMOOTH tool was also used to smooth the summed profiles which removed the white noise from the profile data and increased the SNR.

- **Time of Arrivals (TOAs)**
  In order to obtain DM measurements with better precision, the archives can be divided into a number of frequency bands. The reason for this is that, the SNR would be very low if we used each frequency channel individually. Similarly, for the purpose of improving the period of each observation, the archives can be divided into a number of sub-integrations. At this stage, all observations were split into 10 sub-integrations and 8 frequency bands across the total bandwidth, except the recent observations of German stations (366 frequency channels), which were split into 10 sub-integrations and 6 frequency bands. Also, a number of pulsars were split into only 4 frequency channels due to their overall low SNR. The TOAs were then obtained by using the cross-correlation techniques (see § 2.5.2) between the observations and the generated template. In practise, this process was done by using PAT[1] tool. The result of this process was a single file that contains TOAs of all observations from a corresponding pulsar.

- **Tempo2**
  The aim of this step is to obtain the timing residuals. At this stage, the generated TOAs and the standard template were processed using TEMPO2 which involves

[1] http://psrchive.sourceforge.net/manuals/pat/

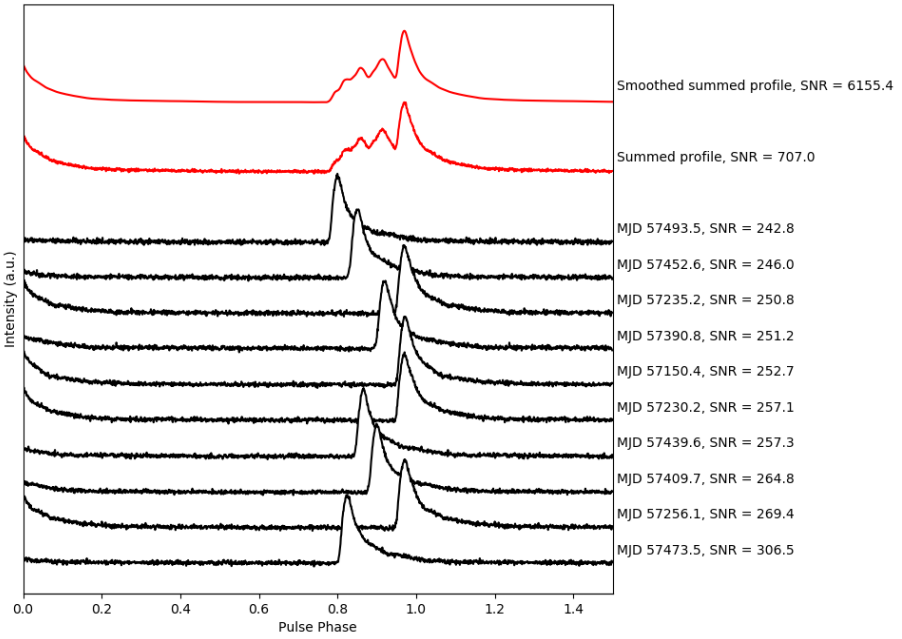

(A)

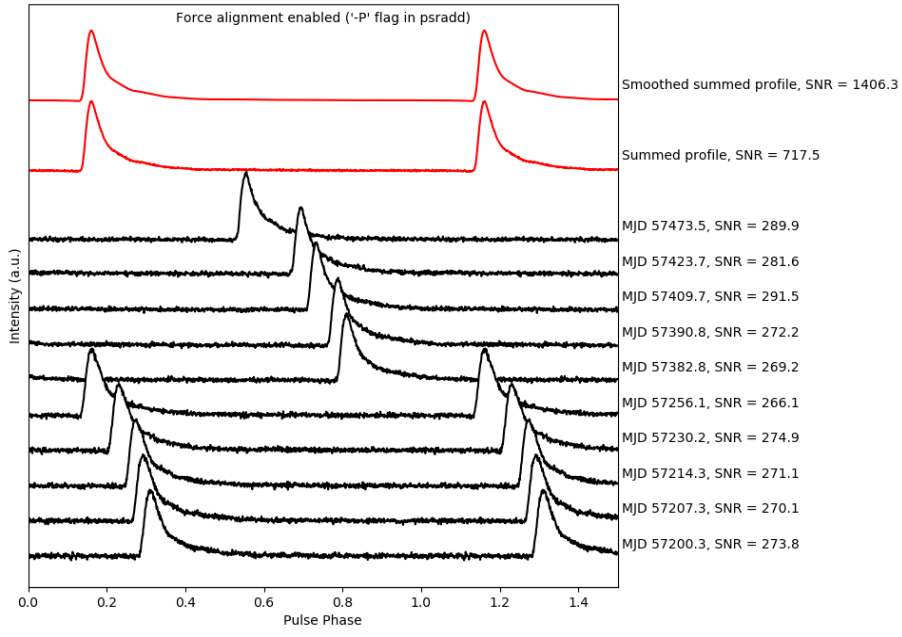

(B)

FIGURE 4.1: The standard profile for J0139+5814 where panel (A) is the initial profile template before applying the alignment which is created by identifying the highest 10 SNR profiles and added to create a single template, then this template is smoothed. Panel (B) is the final profile template which is created by following the same procedure of (A) but forcing the alignment between the profiles.

fitting for a number of parameters. Depending on the pulsar, the fitting for spin frequency (F0), its first derivative (F1) and DM can be sufficient to obtain the timing solution, but for some pulsars, an additional fitting was required e.g. position, proper motion etc, to obtain the desired solution. The final result was new ephemeris that contains improved measurements for DM, period and other parameters. In order to produce a unified version of the ephemeris for all observations, the command: "*tempo2 -gr transform*" was used to transform the version of the ephemeris from TEMPO to TEMPO2.

Second Iteration

At this stage, all the observations were updated using the newly generated ephemeris and then integrated in time and split into 8 sub-bands. The updated data were then used to obtain a standard profile and final TOAs. Also, at this stage, a number of TOAs were identified as clear outliers compared to the rest of TOAs. Each of these outlying TOA was confirmed to be due to the high RFI or low SNR of the observation and subsequently removed from further analysis. Removing these outliers proved to be crucial in achieving better precision of the DM measurements. The final result of this step was a file that contained the DM values for each observation of a particular pulsar. This file was created by using the command: "*tempo2 -gr dm*"

4.2 Results

4.2.1 New Timing Solutions for LOTAS/LOTAAS Sources

During the data reduction steps, I have obtained new timing models for three pulsars: PSRs J0613+3731, J0815+4611 and J1740+27. Investigation of the diagnostic plots for these sources has shown in the sub-integration stack that their periods were wrong such that even within one observation one could see individual sub-integrations pulse profile wrapping in phase. After noticing this, it was clear that this requires additional corrections, by finding the right period within one observation, which was made by using the PSRCHIVE tool PDMP[2]. Then, once the correct period was found, the raw data were re-folded and the timing analysis was repeated. After correcting for the improper period, the data went through my standard timing analysis in order to obtain the DM measurements.

[2] http://psrchive.sourceforge.net/manuals/pdmp/

TABLE 4.1: Result of the new timing solutions obtained in thesis for PSRs J0613+3731, J0815+4611 and J1740+27.

Parameter	**PSR J0613+3731**	**PSR J0815+4611**	**PSR J1740+27**
PSRJ	J0613+3731	J0051+0423	J1740+27
RAJ (h:m:s)	06:13:12.14	08:15:58.00	17:40:32.5763
DECJ (°:′:″)	+37:31:38.2002	+46:11:55.00	+27:15:21.3997
F0 (s^{-1})	1.614991823	2.30286238	0.94499213
F1 (10^{-15} s^{-2})	-8.4464817563(2)	-	-0.196456165(2)
DM ($cm^{-3}pc$)	18.97202	11.274	35.52419
PEPOCH (MJD)	56000.000199	58119.161177	57152.08083

4.2.2 Nulling in PSR J1900+2600

By inspecting the reduced plots for PSR J1900+2600, it became evident that there was no pulsed emission from a number of observations of the source. After inspecting the literature, I found that the pulsar exhibits a nulling behaviour (see Burke-Spolaor et al., 2012). The observations where the pulsar was found to be nulling were removed from further analysis.

4.2.3 DM and DM Derivatives (dDM/dt)

For each pulsar included in this study, I have obtained DM measurements. Figure 4.2 shows the DM variations for PSR J1543-0620 and PSR J2048-1616. The two pulsars showed a clear decreasing trend and a flat trend in their DM measurements, respectively. The scale variations for all pulsars showed different types of variations which is ranging from large-scale variations e.g. PSRs J1136+1551, J1933+2421, J1645-0317 and J1943-1237 to small-scale variations e.g. PSRs J2022+2854, J0826+2637, J1840+5640 and J0332+5434. Some pulsars have also shown more changes from one trend to another along the span of the observation e.g. PSRs J1921+2153, J2157+4017, J1955+5059 and J0837+0610. An example of these pulsars were presented in Figures 4.3. In this figure, PSR J0837+0610 (top panel) shows a clear decreasing trend in early observations with short-term variation in the spread points around MJD 57100 which could be attributed to the underestimation of the DM uncertainties. In the bottom panel, we also see a clear decreasing trend between the points MJD 57000 and 57800.

The DM derivative is the linear change of the DM over the span of the data. Practically, it was determined for each pulsar by applying a linear fit to the DM measurements (See Figure 4.4). The unit of DM derivative is cm^{-3} pc yr^{-1}. Table (4.2) shows the measured values of the DM derivative and their uncertainties for all pulsars included in our study.

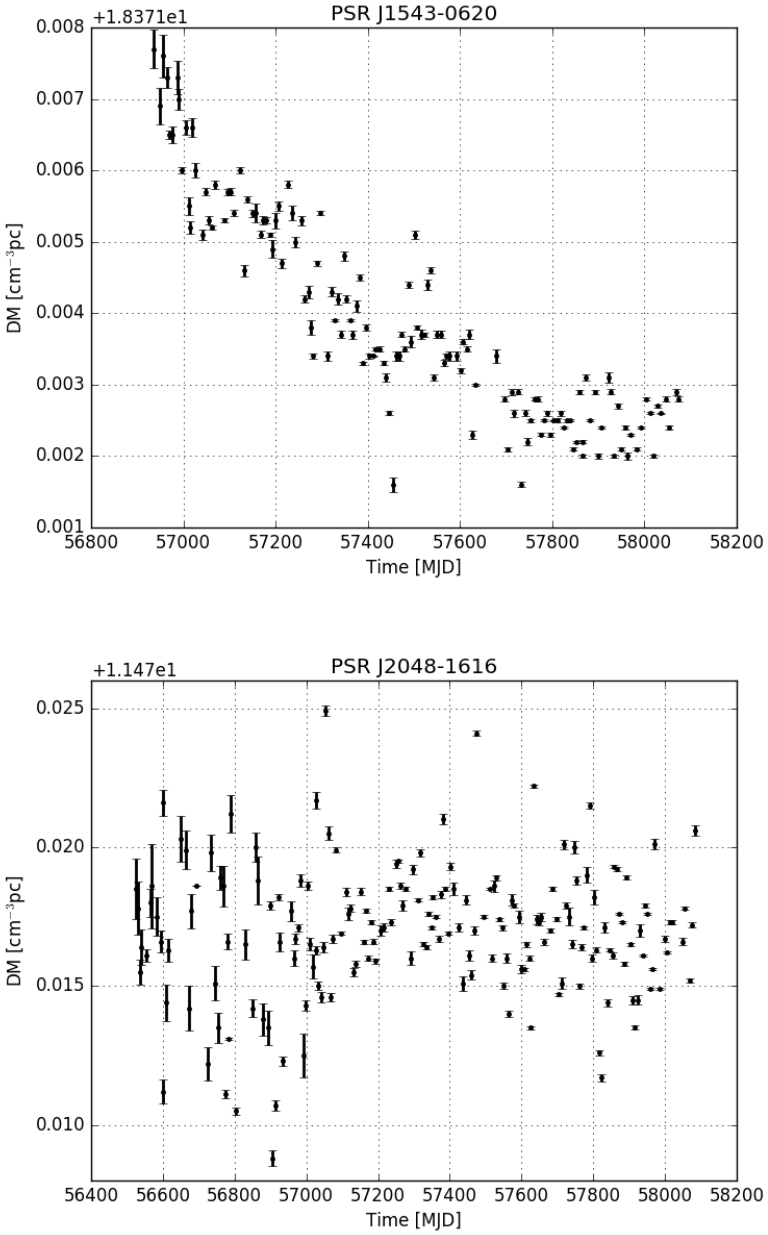

FIGURE 4.2: The DM variation for PSR J1543−0620 and PSR J2048+1616.

Another useful result is to obtain measurements of the correlation between the DM and its derivative. This correlation can be estimated by plotting the DM values against the absolute values of the DM derivative. Then, a linear fit was applied to the plot. This analysis method was first applied by Backer et al. (1993), which they concluded that the absolute value of DM derivative is proportional to the square root of DM. Another study was done by Hobbs et al. (2004) who showed a best fit of,

$$|dDM/dt| \approx 0.0002\sqrt{DM} \text{ cm}^{-3} \text{ pc yr}^{-1}, \tag{4.1}$$

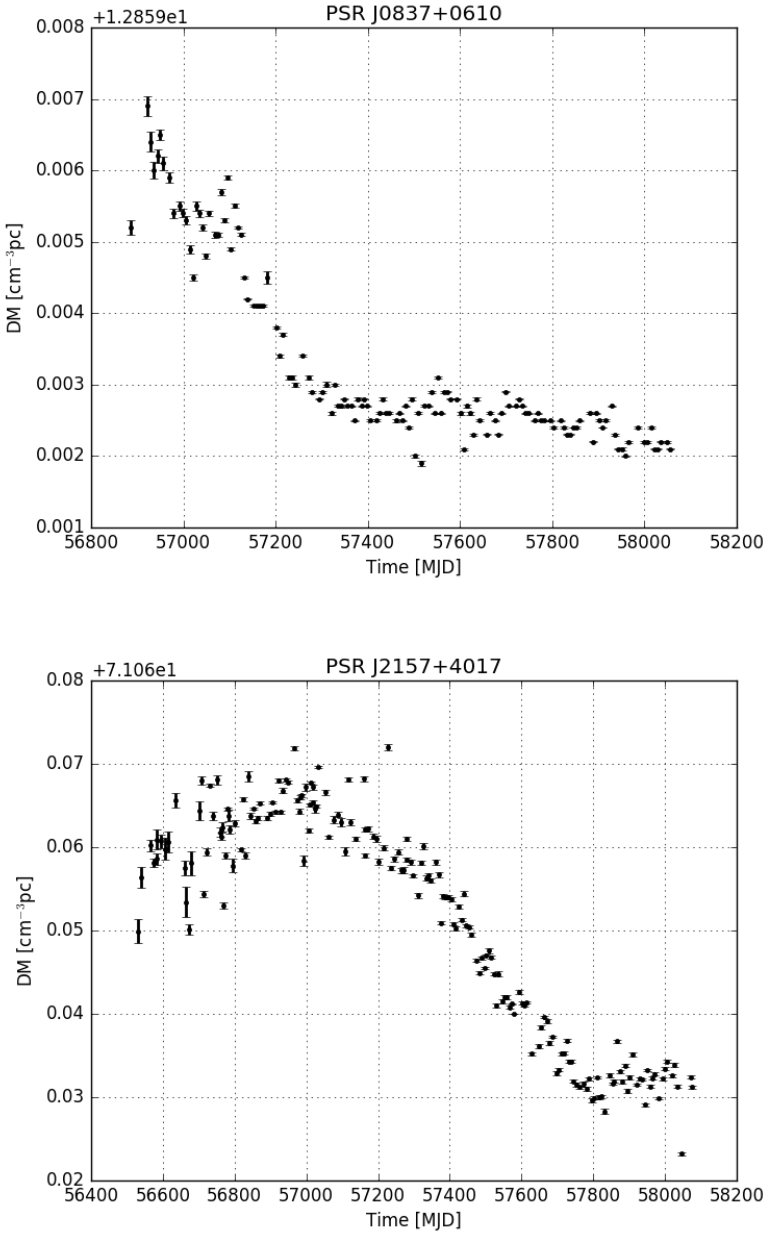

FIGURE 4.3: The DM variation for PSRs J1921+2153 and J2157+4017.

and a gradient of 0.57±0.09.

Following a similar procedure mentioned above, I used the DM and its derivative measured from data to plot the DM values against the absolute values of the DM derivative. I then performed a linear fit to the result. At this stage, I only included the DM derivative values with an uncertainty less than 0.003 (See Figure 4.5). The result of this analysis showed a best fit with a square-root dependence of 0.6±0.2, which is compatible with the value found by Hobbs et al. (2004).

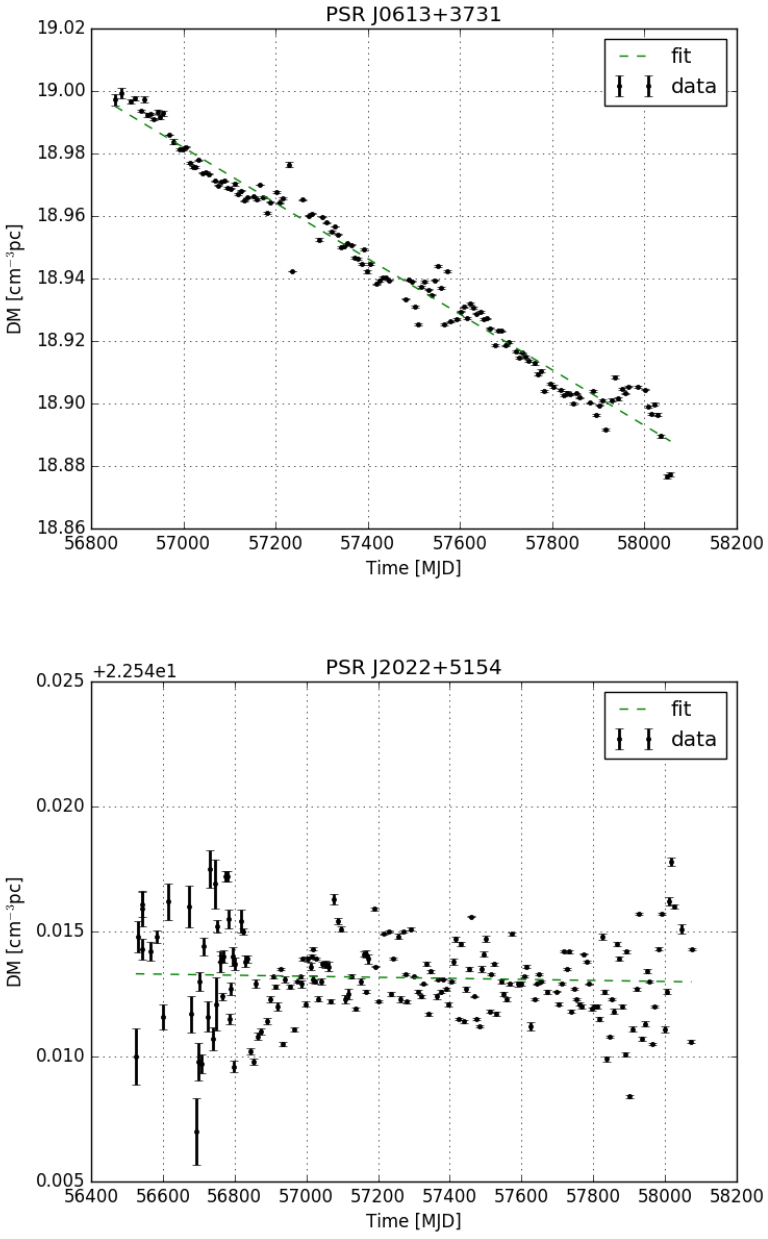

FIGURE 4.4: The DM fitting for PSR J0613+3731 and PSR J2022+5154.

TABLE 4.2: The dispersion measure derivative for pulsars in this study. Where PSR is the name of pulsar, DM Fitting Range is the date range between the first and the last observation of the pulsar in MJD, dDM/dt is the dispersion measure derivative and dDM/dt err is the uncertainty of the DM derivative.

PSR	**DM Fitting Range (MJD)**	**dDM/dt ($cm^{-3}pc/yr$)**	**dDM/dt err**	**PSR**	**DM Fitting Range (MJD)**	**dDM/dt ($cm^{-3}pc/yr$)**	**dDM/dt err**
J0141+6009	56852−58048	0.000 04	0.000 08	J0055+5117	57137−58075	0.000 12	0.001 87
J0323+3944	56887−58048	0.000 67	0.0001	J0108+6608	56539−58048	−0.0010	0.000 33
J0332+5434	56887−58049	0.000 24	0.000 03	J0139+5814	56582−58074	0.000 71	0.000 13
J0454+5543	56887−58056	0.000 02	0.000 03	J0304+1932	56532−58027	0.000 03	0.000 12
J0543+2329#	56887−58056	0.004 92	0.009	J0343+5312	56525−58069	0.001 27	0.001 23
J0613+3731*#	56851−58056	−0.032 50	0.0004	J0358+5413	56542−58076	−0.001 55	0.000 08
J0814+7429	56886−58056	−0.000 19	0.0001	J0406+6138	56699−58074	−0.000 05	0.000 23
J0837+0610	56886−58056	−0.001 15	0.000 06	J0452−1759	56525−58077	0.001 53	0.000 44
J0953+0755	56865−58056	−0.000 06	0.000 04	J0528+2200	56525−57965	0.001 08	0.000 18
J1136+1551	56768−58055	0.000 57	0.000 03	J0614+2229	56570−58047	0.000 15	0.000 12
J1239+2453	56886−58055	−0.000 94	0.000 03	J0629+2415	56524−58075	−0.001 97	0.000 14
J1509+5531	56769−58055	−0.001 18	0.0001	J0820−1350	56532−58075	0.000 82	0.000 13
J1543−0620	56941−57159	−0.003 83	0.0006	J0823+0159	56532−58077	−0.000 44	0.000 24
J1645−0317#	56803−58055	−0.001 04	0.043 17	J0826+2637	56531−57873	−0.000 15	0.000 04
J1740+1311	56863−57964	−0.001 92	0.0002	J0922+0638	57453−58075	0.003 53	0.000 31
J1825−0935	56886−58055	−0.0001	0.0001	J0946+0951	57451−58076	−0.000 31	0.001 48
J1933+2421#	56865−58055	0.023 18	0.086	J1543−0620	56934−58074	−0.001 43	0.000 06
J2018+2839	56886−58055	−0.000 15	0.000 02	J1740+27**	57228−58075	0.001 19	0.000 72
J2113+4644#	56886−57965	−0.034 42	0.153	J1752−2806	56552−58034	0.001 10	0.000 22
J2225+6535	56859−58055	−0.006 56	0.0004	J1820−0427	56531−58074	0.006 42	0.000 52
J2313+4253	56859−58055	0.000 48	0.000 05	J1834−0426	56531−58083	−0.000 01	0.000 26
J0051+0423	57376−58118	−0.000 74	0.0002	J1900−2600	56530−57271	0.001 50	0.001 82
J0102+6537#	57369−58118	−0.008 06	0.003	J1913−0440	56552−58076	−0.007 80	0.000 37

Pulsars excluded from analysis
** LOTAAS discovered
* LOTAS discovered

TABLE 4.3: The dispersion measure derivative for pulsars in this study. Where PSR is the name of pulsar, DM Fitting Range is the date range between the first and the last observation of the pulsar in MJD, dDM/dt is the dispersion measure derivative and dDM/dt err is the uncertainty of the DM derivative.

PSR	**DM Fitting Range (MJD)**	**dDM/dt ($cm^{-3}pc/yr$)**	**dDM/dt err**	**PSR**	**DM Fitting Range (MJD)**	**dDM/dt ($cm^{-3}pc/yr$)**	**dDM/dt err**
J0335+4555	57355−58118	−0.000 06	0.000 13	J1921+2153	56543−58075	−0.000 03	0.000 02
J0540+3207	57376−58118	−0.000 12	0.000 27	J1932+1059	56700−58048	0.000 25	0.000 01
J0546+2441#	57377−58119	−0.191 11	0.486 58	J1935+1616	56532−58076	0.002 61	0.000 33
J0700+6418#	57370−58119	−0.028 21	0.053 79	J1943-1237#	57452−58075	−0.004 11	0.142 43
J0815+4611**	57363−58119	0.000 72	0.000 43	J1948+3540#	57132−58076	−0.009 87	0.006 87
J0921+6254	57363−58119	0.000 22	0.0002	J2022+2854	56573−58076	0.000 19	0.000 02
J1115+5030	57362−58119	0.000 49	0.0003	J2022+5154	56524−58074	−0.000 07	0.0001
J1321+8323	57363−58118	0.000 02	0.000 82	J2048−1616	56524−58082	0.000 12	0.000 14
J1840+5640	57705−58118	−0.000 30	0.000 18	J2219+4754	56531−58075	0.001 34	0.000 04
J2321+6024#	57376−58118	−0.000 36	0.004 04	J2257+5909	56538−58076	0.014 42	0.0008

Pulsars excluded from analysis
** LOTAAS discovered
* LOTAS discovered

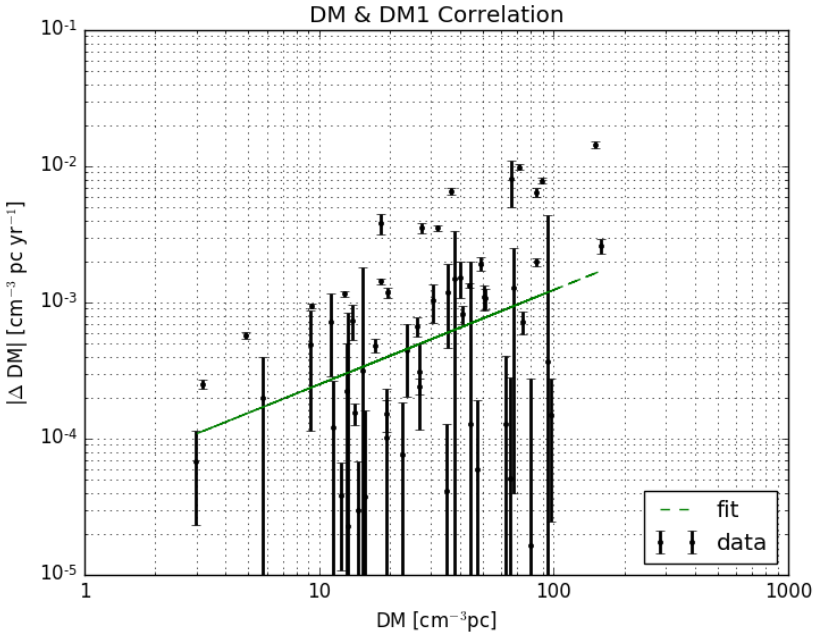

FIGURE 4.5: The correlation between DM and its derivative.

4.2.4 Structure Function

As it was mentioned earlier in § 2.4.3, the structure function, $D_{DM}(\tau)$, is a very useful analysis technique that is used to quantify the turbulent nature of the ISM. It describes the mean-squared variance of the time series for pairs of measurements separated by a time lag (τ). The first attempt of using the structure function to study the DM variations was done by You et al. (2007) as follows,

$$D_{DM}(\tau) = \langle [DM(t+\tau) - DM(t)]^2 \rangle. \tag{4.2}$$

By considering the DM values with different uncertainties, $\sigma_{DM}(\tau)$, Equation (4.2) can be written as:

$$D_{DM}(\tau) = \frac{\sum_i [DM(t_i+\tau) - DM(t_i)]^2 . w_i}{\sum_i w_i}, \tag{4.3}$$

where w_i is the weight, which is given as:

$$w_i = \frac{1}{\sigma^2_{DM}(t+\tau) + \sigma^2_{DM}(t)}. \tag{4.4}$$

For a particular case of the Kolmogorov power-law spectrum, the structure function is represented by,

$$D_{DM}(\tau) = (\tau/\tau_d)^{5/3}. \tag{4.5}$$

Where τ is the time lag and τ_d is the diffractive time scale.

Figure 4.6 shows the result of structure function for PSR J1543−0620, which shows a structure consistent with the Kolmogorov spectrum, starting from the time-lag between 100 and 1000 days. This also indicates the inhomogeneous turbulent structure of the ISM. PSR J0953+0755 shows an inconsistent result compared to the Kolmogorov structure, which could also indicate the presence of the homogeneous structure of the ISM.

After I have obtained the time-dependent DM measurements with their uncertainties, I tried to obtain the structure function directly from these measurements. This can be done by applying an evenly spaced time lag (τ) over the span of the observations and applying Equation (4.2) to obtain the structure function. During the data reductions and analysis, some observations were removed due to many reasons (e.g. RFI, insufficient sub-integrations and frequency channels). As a result of this removal, there were missing values and therefore, it was not possible to generate measurements with an evenly spaced time lag over the span of the observations. In order to solve for this problem, I performed a Gaussian Process (GP) Regression analysis by trying two tools: the PYTHON library GEORGE[3] and GPy[4] (using the radial basis function kernel i.e. RBF kernel), which are both used to obtain a likelihood of the missing part of the data. The predicted measurements are highly dependent on the measured DM and its uncertainty across the span of the data. Using these probabilities to obtain the best estimated values could enable us to create evenly spaced time intervals and associated DM measurements to determine the structure function. However, this approach was unsuccessful, due to the large scattering of the DM measurements as reflected in the uncertainties of the GP output (See Figure 4.7).

4.2.5 DM Variations and the Solar Angle

In pulsar timing, the solar wind can have a significant influence on the measurements of the DM itself. In order to check for this effect, I first assumed an angular distance from the Sun <= 20° for observations which could be affected by the solar wind. Next, for

[3] https://george.readthedocs.io/en/latest/
[4] http://sheffieldml.github.io/GPy/

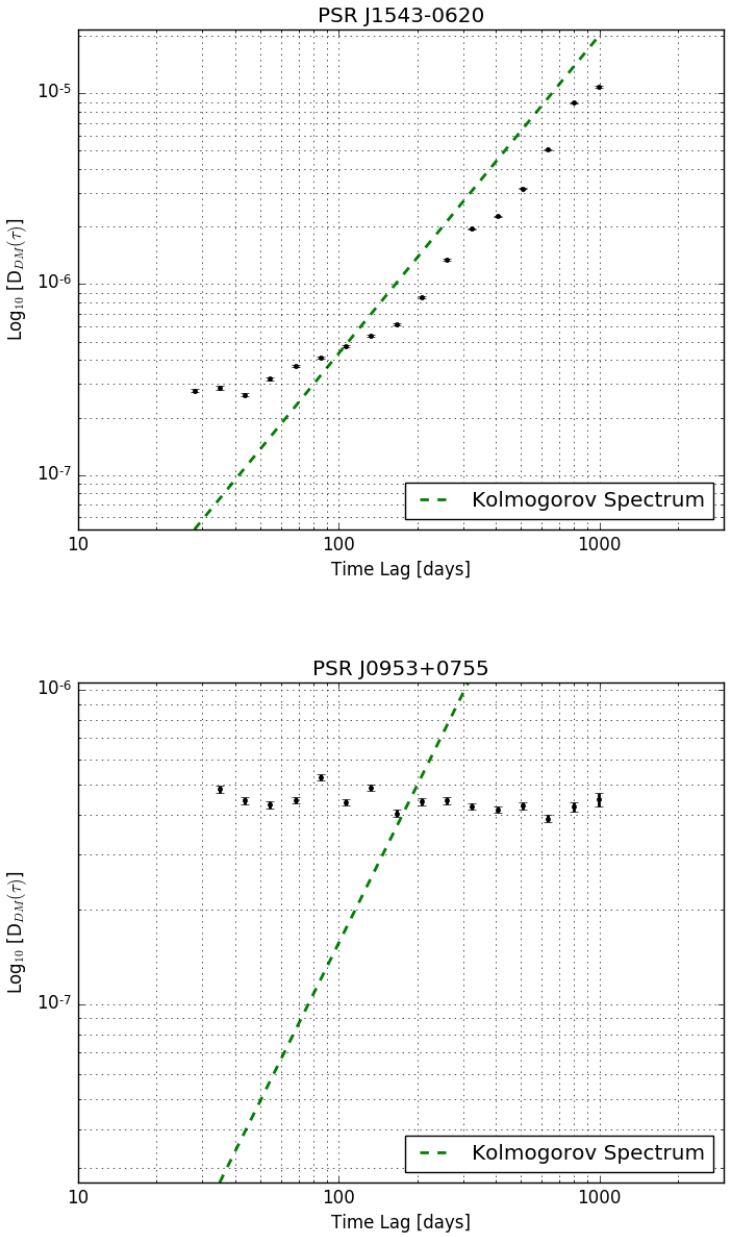

FIGURE 4.6: The DM structure function for PSR J1543−0620 and PSR J0953+0755.

each observation, I calculated the solar angle, then plotted it with the corresponding DM values. Inspection of those plots revealed that there was no significant influence of the solar wind on my DM measurements. Figure 4.8 shows an example of the observations of PSR J0614+2229.

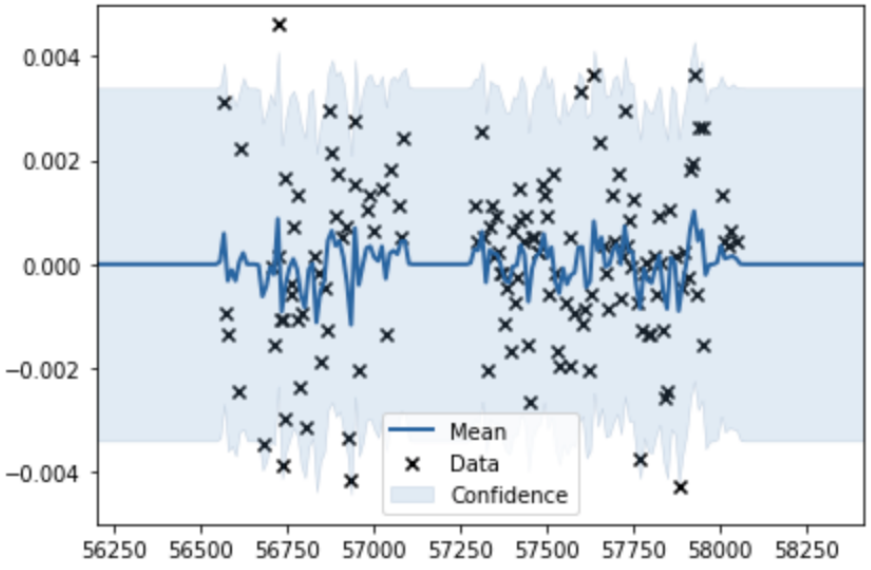

FIGURE 4.7: The result of GPy framework which is used to generate a Gaussian Process (GP) model for the DM measurements. The result shows large uncertainties due to the scattering of the the DM values for PSR J1543−0620.

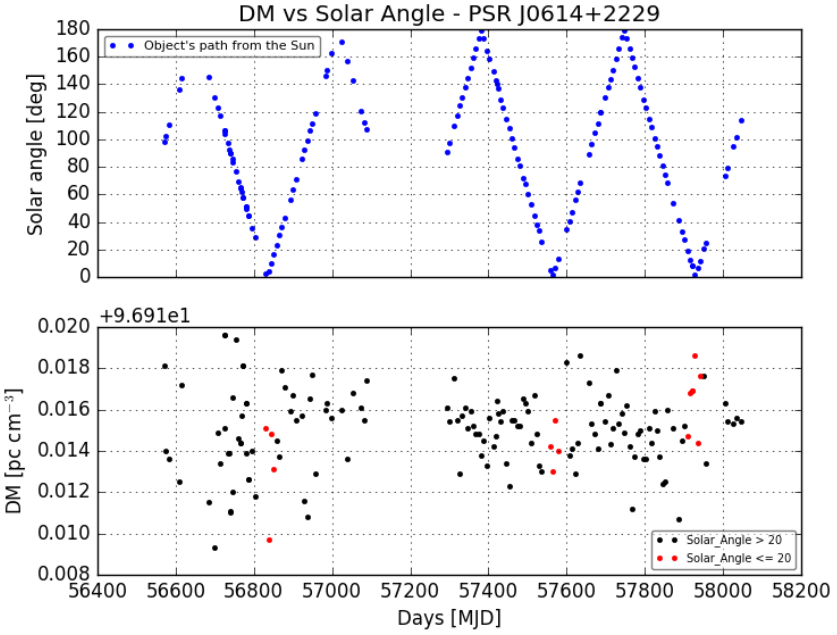

FIGURE 4.8: The Solar angle between the Sun and PSR J0614+2229 compared with the DM measurements.

Chapter 5

Discussion and Conclusions

- The purpose of this thesis was to present results from the study of the DM variations for a large sample of sources (68 pulsars) observed over a period of 3.5 years. The data were obtained from six International LOFAR Stations which are located in France, Germany and Sweden.
- I have obtained the DM measurements for each pulsar by using timing analysis techniques. Then, the structure function was calculated using these measurements to study the general properties of the ISM. Additionally, I have checked the influence of the solar wind on the DM measurements.
- The results of this study have shown that the DM variations are ranging from large-scale variations to small-scale variations over the span of the data. It's important to note that, although the general trends which are seen in the DM variations are considered a convincing result, the small-scale DM variations require more investigations and examinations in order for them to be considered credible. I identify that as due to the technique with which the TOAs were estimated for each pulsar. This could be corrected by carefully applying different approaches to data analysis for each source (priv. comm. G. M. Shaifullah)
- The result of the DM structure function shows that the variations of the DM measurements for a number of pulsars were consistent with the theoretical model of the Kolmogorov power spectrum, which is used to describe the turbulence nature of the interstellar medium.
- During the structure function analysis, I started to look into obtaining direct measurements of structure function from the DM variations by applying the Gaussian Process (GP) Regression analysis, but this turned out to be unsuccessful attempt.

This is most likely due to the aforementioned TOAs error measurements and after appropriate improvements deserve its own study.

- I have also calculated the correlations between the DM and their derivatives. The obtained result of this correlation was shown a square-root dependence of 0.6 ± 0.2 which is comparable with the previously published results (e.g. Hobbs et al., 2004).

- One of the major results of my study was obtaining new timing solutions for three pulsars: PSRs J0613+3731, J0815+4611 and J1740+27. These improved solutions can be used in ongoing observations with e.g. LOFAR Core or International LOFAR Stations.

- I have prepared an automated data reduction pipeline which was invaluable given the large amount of observations to process. For some pulsars, data analysis result have shown that to have that an individual approach is required in order to process them correctly (e.g. the polarization calibration techniques presented in Tiburzi et al. (submitted) and Donner et al. (in prep)). These approaches are out of the scope of this study.

- Typical publications of DM variations use data over $5-6$ years as a minimum time span. There is already a larger sample of pulsar observations, including millisecond pulsars (MSPs), taken over longer period of time (i.e. 5 years) compared to what was used during this study. For future studies these observations could be used to obtain a higher quality result. Additionally, there is a wealth of information that can be learned by trying the low-frequency observations from LOFAR with the higher frequency observations from a telescope like the Westerbork Synthesis Radio Telescope (WSRT), which observed sources in P band (i.e. 250 to 500 MHz) and L band (i.e. 0.5 to 1.5 GHz) (See Karuppusamy et al. 2008). This ultimately could enable us to improve DM measurements as well as timing analysis of selected sources observed by both telescopes.

Bibliography

Armstrong, J., Rickett, B., and Spangler, S. (1995). Electron density power spectrum in the local interstellar medium. *The Astrophysical Journal*, 443:209–221.

Baade, W. and Zwicky, F. (1934). Remarks on super-novae and cosmic rays. *Physical Review*, 46(1):76.

Backer, D., Hama, S., Van Hook, S., and Foster, R. (1993). Temporal variations of pulsar dispersion measures. *The Astrophysical Journal*, 404:636–642.

Backer, D. C., Kulkarni, S. R., Heiles, C., Davis, M., and Goss, W. (1982). A millisecond pulsar. *Nature*, 300(5893):615–618.

Bailes, M., Barr, E., Bhat, N., Brink, J., Buchner, S., Burgay, M., Camilo, F., Champion, D., Hessels, J., Janssen, G., et al. (2018). Meertime-the meerkat key science program on pulsar timing. *arXiv preprint arXiv:1803.07424*.

Burgay, M., D'amico, N., Possenti, A., Manchester, R., Lyne, A., Joshi, B., McLaughlin, M., Kramer, M., Sarkissian, J., Camilo, F., et al. (2003). An increased estimate of the merger rate of double neutron stars from observations of a highly relativistic system. *Nature*, 426(6966):531–533.

Burke-Spolaor, S., Johnston, S., Bailes, M., Bates, S., Bhat, N., Burgay, M., Champion, D., D'Amico, N., Keith, M., Kramer, M., et al. (2012). The high time resolution universe pulsar survey–v. single-pulse energetics and modulation properties of 315 pulsars. *Monthly Notices of the Royal Astronomical Society*, 423(2):1351–1367.

Camilo, F., Ransom, S. M., Halpern, J. P., Reynolds, J., Helfand, D. J., Zimmerman, N., and Sarkissian, J. (2006). Transient pulsed radio emission from a magnetar. *Nature*, 442(7105):892–895.

Coenen, T., Van Leeuwen, J., Hessels, J. W., Stappers, B. W., Kondratiev, V. I., Alexov, A., Breton, R., Bilous, A., Cooper, S., Falcke, H., et al. (2014). The lofar pilot surveys for pulsars and fast radio transients. *Astronomy & astrophysics*, 570:A60.

Cordes, J. M., Shannon, R. M., and Stinebring, D. R. (2016). Frequency-dependent dispersion measures and implications for pulsar timing. *The Astrophysical Journal*, 817(1):16.

Dabrowski, B. P., Krankowski, A., Baszkiewicz, L., and Rothkaehl, H. (2016). Prospects for solar and space weather research with polish part of the lofar telescope. *Acta Geophysica*, 64(3):825–840.

Donner, J. (2017). Lofar studies of the ionised interstellar medium at the smallest scales.

Duncan, R. C. and Thompson, C. (1992). Formation of very strongly magnetized neutron stars-implications for gamma-ray bursts. *The Astrophysical Journal*, 392:L9–L13.

Edwards, R. T., Hobbs, G., and Manchester, R. (2006). tempo2, a new pulsar timing package–ii. the timing model and precision estimates. *Monthly Notices of the Royal Astronomical Society*, 372(4):1549–1574.

Field, G., Goldsmith, D., and Habing, H. (1969). Cosmic-ray heating of the interstellar gas. *The Astrophysical Journal*, 155:L149.

Goldreich, P. and Julian, W. H. (1969). Pulsar electrodynamics. *The Astrophysical Journal*, 157:869.

Gunn, J. and Ostriker, J. (1970). On the nature of pulsars. iii. analysis of observations. *The Astrophysical Journal*, 160:979.

Harding, A. K. (2013). The neutron star zoo. *Frontiers of Physics*, 8(6):679–692.

Hessels, J. W., Ransom, S. M., Stairs, I. H., Freire, P. C., Kaspi, V. M., and Camilo, F. (2006). A radio pulsar spinning at 716 hz. *Science*, 311(5769):1901–1904.

Hewish, A., Bell, S. J., Pilkington, J., Scott, P. F., and Collins, R. A. (1968). Observation of a rapidly pulsating radio source. *Nature*, 217(5130):709–713.

Hobbs, G. (2009). Pulsar timing array projects. *Proceedings of the International Astronomical Union*, 5(S261):228–233.

Hobbs, G., Archibald, A., Arzoumanian, Z., Backer, D., Bailes, M., Bhat, N., Burgay, M., Burke-Spolaor, S., Champion, D., Cognard, I., et al. (2010). The international pulsar timing array project: using pulsars as a gravitational wave detector. *Classical and Quantum Gravity*, 27(8):084013.

Hobbs, G., Edwards, R., and Manchester, R. (2006). Tempo2, a new pulsar-timing package–i. an overview. *Monthly Notices of the Royal Astronomical Society*, 369(2):655–672.

Hobbs, G., Lyne, A., Kramer, M., Martin, C., and Jordan, C. (2004). Long-term timing observations of 374 pulsars. *Monthly Notices of the Royal Astronomical Society*, 353(4):1311–1344.

Hotan, A. W., Van Straten, W., and Manchester, R. (2004). Psrchive and psrfits: an open approach to radio pulsar data storage and analysis. *Publications of the Astronomical Society of Australia*, 21(3):302–309.

Karuppusamy, R., Stappers, B., and Van Straten, W. (2008). Puma-ii: a wide band pulsar machine for the westerbork synthesis radio telescope. *Publications of the Astronomical Society of the Pacific*, 120(864):191.

Keane, E. F. (2010). *The Transient Radio Sky*. PhD thesis, University of Manchester.

Lattimer, J. and Prakash, M. (2001). Neutron star structure and the equation of state. *The Astrophysical Journal*, 550(1):426.

Lazarus, P., Karuppusamy, R., Graikou, E., Caballero, R., Champion, D., Lee, K., Verbiest, J., and Kramer, M. (2016). Prospects for high-precision pulsar timing with the new effelsberg psrix backend. *Monthly Notices of the Royal Astronomical Society*, 458(1):868–880.

Lewin, W. and Van der Klis, M. (2006). *Compact stellar X-ray sources*, volume 39. Cambridge University Press.

Lorimer, D. R. (2001). Binary and millisecond pulsars at the new millennium. *Living Reviews in Relativity*, 4(1):5.

Lorimer, D. R. and Kramer, M. (2005). *Handbook of pulsar astronomy*. Cambridge University Press.

Lyne, A. and Graham-Smith, F. (2012). *Pulsar astronomy*. Number 48. Cambridge University Press.

Lyne, A. and Lorimer, D. (1994). High birth velocities of radio pulsars. *Nature*, 369(6476):127–129.

Manchester, R. (2017). Pulsar timing and its applications. In *Journal of Physics: Conference Series*, volume 932, page 012002. IOP Publishing.

Manchester, R. N., Hobbs, G. B., Teoh, A., and Hobbs, M. (2005). The Australia Telescope National Facility Pulsar Catalogue. *aj*, 129:1993–2006.

McKay-Bukowski, D., Vierinen, J., Virtanen, I. I., Fallows, R., Postila, M., Ulich, T., Wucknitz, O., Brentjens, M., Ebbendorf, N., Enell, C.-F., et al. (2015). Kaira:

The kilpisjärvi atmospheric imaging receiver array—system overview and first results. *IEEE Transactions on Geoscience and Remote Sensing*, 53(3):1440–1451.

McKee, C. F. and Ostriker, J. P. (1977). A theory of the interstellar medium-three components regulated by supernova explosions in an inhomogeneous substrate. *The Astrophysical Journal*, 218:148–169.

McLaughlin, M. A., Lyne, A., Lorimer, D., Kramer, M., Faulkner, A., Manchester, R., Cordes, J., Camilo, F., Possenti, A., Stairs, I., et al. (2006). Transient radio bursts from rotating neutron stars. *Nature*, 439(7078):817–820.

Olausen, S. and Kaspi, V. (2014). The mcgill magnetar catalog. *The Astrophysical Journal Supplement Series*, 212(1):6.

Oppenheimer, J. R. and Volkoff, G. M. (1939). On massive neutron cores. *Physical Review*, 55(4):374.

Pacini, F. (1967). Energy emission from a neutron star. *Nature*, 216(5115):567–568.

Pitkin, M. (2018). psrqpy: a python interface for querying the ATNF pulsar catalogue. *Journal of Open Source Software*, 3(22):538.

Rickett, B. J. (1990). Radio propagation through the turbulent interstellar plasma. *Annual review of astronomy and astrophysics*, 28(1):561–605.

Ruderman, M. A. and Sutherland, P. G. (1975). Theory of pulsars-polar caps, sparks, and coherent microwave radiation. *The Astrophysical Journal*, 196:51–72.

Stappers, B., Hessels, J., Alexov, A., Anderson, K., Coenen, T., Hassall, T., Karastergiou, A., Kondratiev, V., Kramer, M., Van Leeuwen, J., et al. (2011). Observing pulsars and fast transients with lofar. *Astronomy & astrophysics*, 530:A80.

Sturrock, P. (1971). A model of pulsars. *The Astrophysical Journal*, 164:529.

Taylor, J. H. (1992). Pulsar timing and relativistic gravity. *Phil. Trans. R. Soc. Lond. A*, 341(1660):117–134.

Taylor, J. H. and Weisberg, J. M. (1982). A new test of general relativity-gravitational radiation and the binary pulsar psr 1913+ 16. *The Astrophysical Journal*, 253:908–920.

Tyul'bashev, S. A., Tyul'bashev, V. S., and Malofeev, V. M. (2018). Detection of 25 new rotating radio transients at 111 mhz. *arXiv preprint arXiv:1807.07565*.

van Haarlem, M. a., Wise, M., Gunst, A., Heald, G., McKean, J., Hessels, J., De Bruyn, A., Nijboer, R., Swinbank, J., Fallows, R., et al. (2013). Lofar: The low-frequency array. *Astronomy & Astrophysics*, 556:A2.

Verbiest, J., Lentati, L., Hobbs, G., van Haasteren, R., Demorest, P. B., Janssen, G., Wang, J.-B., Desvignes, G., Caballero, R., Keith, M., et al. (2016). The international pulsar timing array: first data release. *Monthly Notices of the Royal Astronomical Society*, 458(2):1267–1288.

Wielebinski, R. (2002). The Characteristics of (Normal) Pulsars. In Becker, W., Lesch, H., and Trümper, J., editors, *Neutron Stars, Pulsars, and Supernova Remnants*, page 167.

Williamson, I. P. (1972). Pulse broadening due to multiple scattering in the interstellar medium. *Monthly Notices of the Royal Astronomical Society*, 157(1):55–71.

You, X.-P., Hobbs, G., Coles, W. A., Manchester, R. N., Edwards, R., Bailes, M., Sarkissian, J., Verbiest, J. P., Van Straten, W., Hotan, A., et al. (2007). Dispersion measure variations and their effect on precision pulsar timing. *Monthly Notices of the Royal Astronomical Society*, 378(2):493–506.

Zarka, P., Tagger, M., Denis, L., Girard, J., Konovalenko, A., Atemkeng, M., Arnaud, M., Azarian, S., Barsuglia, M., Bonafede, A., et al. (2015). Nenufar: Instrument description and science case. In *Antenna Theory and Techniques (ICATT), 2015 International Conference on*, pages 1–6. IEEE.